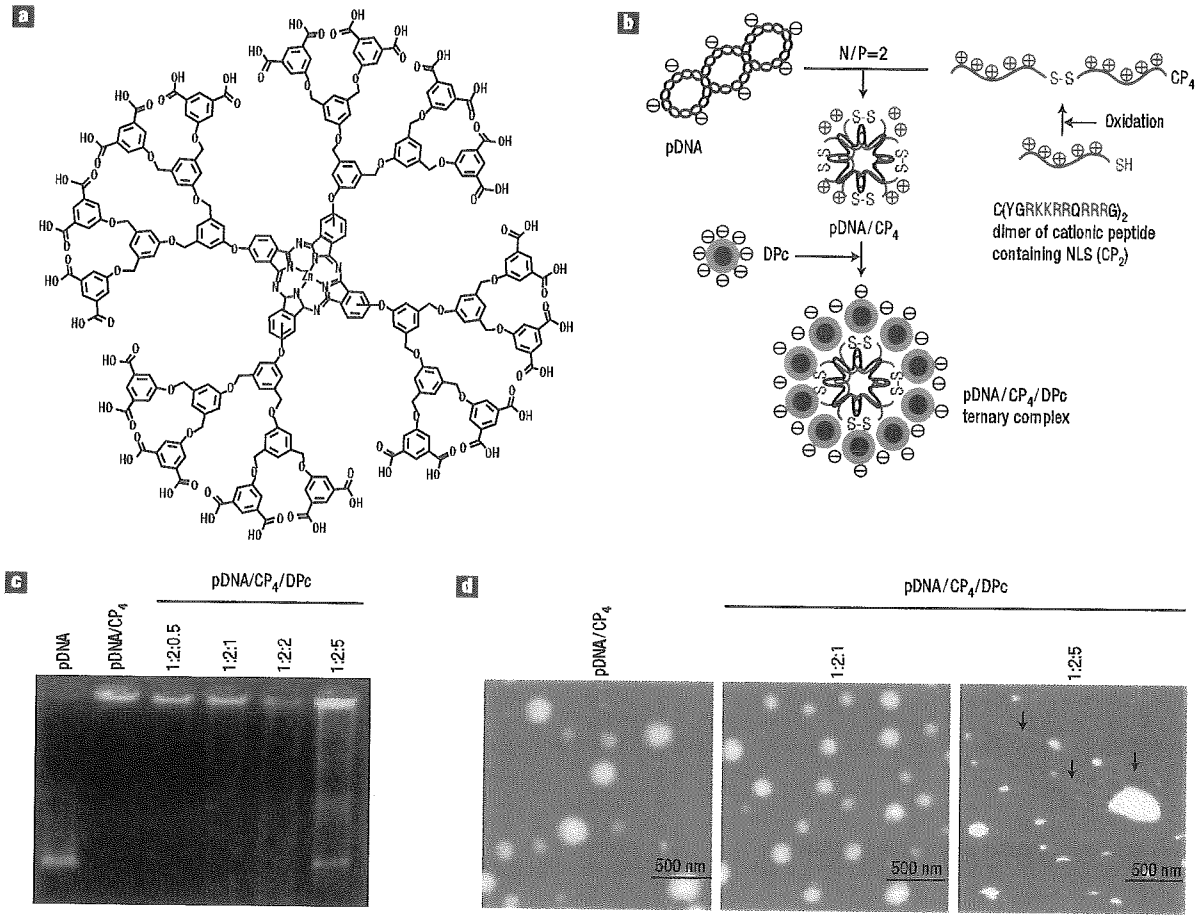

Figure 1 Preparation and characterization of the ternary complex. a, The chemical structure of ionic DPc. **b**, A scheme for preparation of the pDNA/CP_4/DPc ternary complex. **c**, Gel retardation assay of the pDNA/CP_4 polyplex prepared at an N/P ratio of 2, and the ternary complexes with varying charge molar ratios of pDNA/CP_4/DPc. **d**, AFM images of the pDNA/CP_4 and pDNA/CP_4/DPc complexes. Arrow heads indicate plasmid DNA released from the ternary complexes.

for *in vivo* applications. From the viewpoint of materials science, this concept can be integrated into nanodevices for drug and gene delivery.

In the present paper, we assume that the control of subcellular localization of photosensitizers may be a key to the PCI-mediated gene delivery with reduced cytotoxicity, because the photodamage to sensitive organelles other than the endosomal membrane, for example the plasma and mitochondrial membranes, might be responsible for the photocytotoxicity[11]. In addition, gene carriers should be equipped with a photosensitizing unit as one component for *in vivo* applications. These assumptions motivated us to develop a light-responsive gene carrier based on a ternary complex of pDNA, cationic peptides and anionic dendrimer-based photosensitizers (dendrimer phthalocyanine: DPc; Fig. 1a). Dendrimers, the three-dimensional tree-like branched macromolecules, have attracted growing interest as materials for drug and gene delivery[12–16], and the ternary complex is a different biomedical application of dendrimers. The ternary complex has shown significant photochemical enhancement of the transgene expression *in vitro* with reduced photocytotoxicity and *in vivo* gene transfer to the conjunctival tissue in the rat eye in a light-selective manner.

The ternary complex is composed of a core of a pDNA/cationic polymer polyplex enveloped with anionic DPc (Fig. 1a) as illustrated in Fig. 1b. DPc possesses a centre phthalocyanine molecule surrounded by a second generation of aryl ether dendrons, and 32 carboxyl groups on the periphery of DPc allow polyion complex formation with cationic polyplexes. In the present study, the core polyplex was formed from a quadruplicated cationic peptide (CP_4), where a peptide (CP_2: C(YGRKKRRQRRRG)$_2$)) was dimerized through a disulphide linkage, and pDNA was mixed with the CP_4 peptide at a molar ratio of cationic amino acids to a phosphate anion in DNA (N/P ratio) of 2. It has been demonstrated[17] that CP_2 and CP_4 contain a nuclear localization sequence (NLS) and thereby effectively mediate the gene transfection to the cell with the aid of conventional transfection reagents such as PEI and LipofectAMINE to promote the endosomal escape of the polyplex. Thus, these potent cationic peptides were used for the formation of the ternary complex to ensure the efficient gene transfection following the endosomal escape of the polyplex.

In this study, the ternary complexes were prepared by varying the charge molar ratios of pDNA/CP_4/DPc, and the complex formation was confirmed by a gel retardation assay (Fig. 1c). As a result, pDNA was incorporated into the complexes with charge ratios up to 1:2:2, but was excluded from the complex with a charge ratio of 1:2:5. The release of pDNA from the 1:2:5 complex was also observed by atomic force microscopy (AFM) as shown in Fig. 1d.

Table 1 Size, size distribution and ζ-potential of the electrostatic assemblies containing plasmid DNA.

	Cumulant diameter (nm)	Polydispersity index	ζ-potential (mV)
pDNA/PEI (1:10)	127.8	0.211	23.8±0.1
pDNA/CP_4 (1:2)	100.8	0.185	21.3±2.3
pDNA/CP_4/DPc (1:2:0.5)	149.7	0.115	−8.5±3.6
pDNA/CP_4/DPc (1:2:1)	130.8	0.108	−29.2±2.6
pDNA/CP_4/DPc (1:2:2)	107.7	0.143	−23.2±0.9
pDNA/CP_4/DPc (1:2:5)	267.1	0.180	−49.6±0.7
pDNA/CP_4/PAA* (1:2:0.5)	621.2	0.444	−27.1±0.8
pDNA/CP_4/PAA (1:2:1)	672.0	0.477	−25.8±0.4
pDNA/CP_4/PAA (1:2:2)	912.3	0.361	−24.3±0.8
pDNA/CP_4/PAA (1:2:5)	1426	0.278	−25.3±2.3

* PAA: Poly(aspartic acid) homopolymer with a polymerization degree of 26

Thus, addition of excess DPc might disintegrate the pDNA/CP_4 polyplex. The size, polydispersity index and ζ-potential of the pDNA/CP_4/DPc ternary complexes are summarized in Table 1. The addition of DPc to the positively charged pDNA/CP_4 polyplex gave negative ζ-potential values, suggesting the formation of ternary complexes covered with anionic DPc. A decrease in the size of the ternary complexes with increasing DPc ratios may be attributed to shrinkage of the cationic peptide corona on the polyplex surface through electrostatic interaction with DPc. Surface modification with anionic DPc provided the 1:2:1 and 1:2:2 complexes with excellent colloidal stability, whereas the 1:2:0.5 complex possessing an almost neutral ζ-potential value tended to precipitate in several hours. Significantly, the ternary complexes showed much lower polydispersity indices compared with the pDNA/CP_4 or PEI polyplexes (Table 1). The AFM observation has revealed consistently that the 1:2:1 complex consists of spherical particles with a narrow size distribution, which is in marked contrast to the pDNA/CP_4 polyplex containing large aggregates (Fig. 1d). Note that the addition of poly(aspartic acid) (PAA) homopolymer with a polymerization degree of 26 to the pDNA/CP_4 polyplex resulted in a large aggregate formation (Table 1). Hence, the three-dimensional structure of DPc is assumed to play an essential role in the formation of a ternary complex with a narrow size distribution and excellent colloidal stability. The layer-by-layer assemblies of oppositely charged polyelectrolytes onto colloidal particles have attracted considerable attention[18,19]; however, the pDNA/CP_4/DPc ternary complex is definitely discriminated from the layer-by-layer assemblies, because a core composed of hard materials is not required for the formation of the ternary complex. Thus, the ternary complex presented here is a supramolecular assembly consisting of a pDNA/CP_4 polyplex core and a DPc envelope.

The properties of DPc and the ternary complex related to the initial steps in the gene transfection to the cell (that is, processes from the cellular uptake to when photodamage to the endosomal membrane occurred) were evaluated, because the ternary complex was designed to control these processes. First, the cellular uptake of the ternary complex was evaluated by flow cytometry using a fluorescein-labelled pDNA, as shown in Fig. 2a. The amount of cellular uptake of the ternary complexes was less than that of cationic polyplexes such as pDNA/CP_4 and pDNA/PEI, and decreased as the DPc ratio increased. The ternary complex covered with anionic DPc should have a lower affinity for the negatively charged plasma membrane of cells, accounting for the results in Fig. 2a.

The pH-dependent hydrophilic/hydrophobic behaviour of DPc and its possible interaction with cell membranes was estimated by octanol/water partitioning, which is a common method for evaluation of drug–membrane interactions[20]. The partitioning (%) of DPc to the octanol phase increased as the pH decreased to 5.0–5.5 (Fig. 2b), suggesting the increased hydrophobicity of DPc and possible interactions with cell membranes under low-pH conditions. Because the DPc consists of a hydrophobic dendritic framework, the protonation of the peripheral carboxyl group under acidic conditions might increase its hydrophobicity. This result suggests that DPc may be released from the ternary complex under endosomal pH conditions to interact with the endosomal membrane, while electrostatically interacting with the positively charged surface of the polyplex at physiological pH. This assumption offers an interesting opportunity to selectively photodamage the endosomal membrane for effective PCI.

Figure 2c shows the subcellular distribution of FITC-labelled dextran co-incubated with the 1:2:1 ternary complex. It was demonstrated that FITC-dextran showed diffused fluorescence throughout the cytoplasm after photoirradiation, whereas it showed punctuated fluorescence corresponding to localization in the endosome and/or lysosome before photoirradiation. This result suggests the capability of the ternary complex of releasing the contents in the vesicular organelles to the cytoplasm on photoirradiation.

To evaluate the potential of the ternary complex for PCI-mediated gene delivery, *in vitro* transfection experiments were performed on HeLa cells with a luciferase (Luc) reporter gene in the presence or absence of photoirradiation. Simultaneously, the cell viability was assessed by MTT assay (see Methods). Figure 3a shows the transfection efficiency and cytotoxicity of the pDNA/CP_4 polyplex and pDNA/CP_4/DPc ternary complexes with varying charge ratios of DPc after irradiation of the light with increasing fluence. In this experiment, the cells were photoirradiated after 6-h incubation with each complex and fresh medium replacement, followed by 48-h post-incubation. The 1:2:1 and 1:2:2 ternary complexes achieved more than 100-fold photochemical enhancement of the transgene expression with minimal photocytotoxicity over a wide range of fluence (−3.6 J cm^{-2}), whereas the 1:2:5 ternary complex, having a disordered structure, showed the lowest transfection activity (Fig. 3a). Note that a further increase in fluence resulted in a significant increase in the photocytotoxicity of the ternary complexes (a 50–70% decrease in the viability at 5.4 J cm^{-2}; see Supplementary Information, Fig. S1). The transfection to a different cell line (that is, 293T cells) revealed similar photochemical enhancement of transgene expression by the ternary complexes, although the 1:2:1 and 1:2:2 ternary complexes showed appreciable photocytotoxicity at a fluence higher than 2.7 J cm^{-2} (see Supplementary Information, Fig. S2A). Furthermore, when HeLa cells were incubated with the ternary complexes for a prolonged period (that is, 24 h) before photoirradiation, the results were similar to those in Fig. 3a (see Supplementary Information, Fig. S2B). The effect of PCI-mediated transfection was comparable to or more effective than that of hydroxychloroquine, a potent endosomotropic agent[21], depending on the cell lines (see Fig. 3a and Supplementary Information, Fig. S2A).

The effect of the ternary complex on the PCI-mediated transfection was further compared with that of $AlPcS_{2a}$ (aluminium phthalocyanine with two sulphonate groups on adjacent phthalate rings), which was demonstrated to be an effective photosensitizer in PCI[8–10]. Figure 3b shows the effect of $AlPcS_{2a}$ on the transfection efficiency of the pDNA/CP_4 polyplex (N/P ratio = 2) and cytotoxicity to HeLa cells with varying concentrations of $AlPcS_{2a}$ and fluence. In the system using $AlPcS_{2a}$, the photochemical enhancement of the transfection was accompanied by a significant increase in the photocytotoxicity, regardless of the concentrations of $AlPcS_{2a}$. Comparison between Fig. 3a and b reveals that the ternary complex achieved an expanded range of safe light doses,

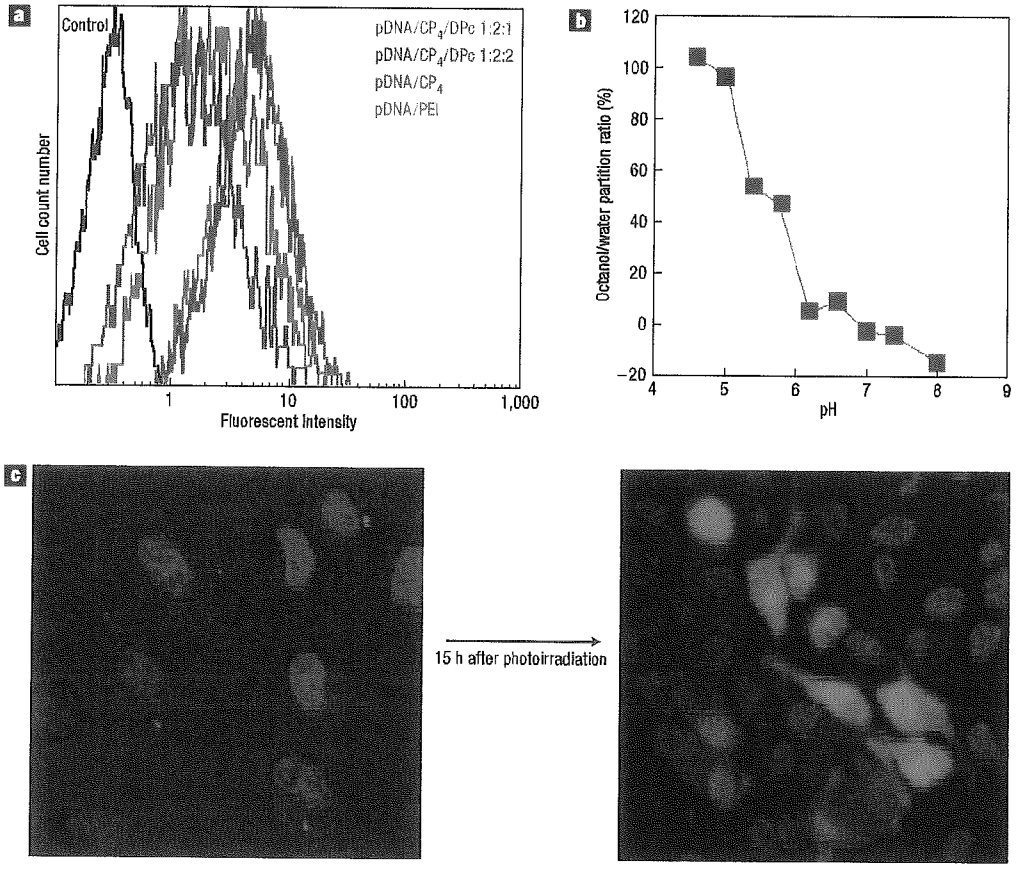

Figure 2 Properties of DPc and the pDNA/CP_4/DPc ternary complexes. a, Cellular uptake of the electrostatic complexes incorporating fluorescein-labelled pDNA. HeLa cells were incubated with each complex for 6 h, followed by flow cytometric analysis. The pDNA/PEI polyplex was prepared at an N/P ratio of 10. **b**, The pH-dependent partitioning (%) of DPc from the aqueous phase to the octanol phase. **c**, The intracellular distribution of FITC-dextran (green) co-incubated with the pDNA/CP_4/DPc complex with a charge ratio of 1:2:1 before and after photoirradiation. HeLa cells were incubated with the ternary complex for 6 h, followed by photoirradiation. The cell nuclei were stained with Hoechst 33258 (blue).

in which remarkable photochemical enhancement of the transgene expression was accomplished without compromising cell viability, ensuring the safety and effectiveness of the PCI-mediated *in vivo* gene delivery.

The reduced cytotoxicity after prolonged incubation with synthetic vectors might be one of the main criteria for successful *in vivo* transfection. In this study, the cells were photoirradiated after 6 h incubation with each complex, followed by 48-h post-incubation without medium replacement. Figure 3c shows the transfection efficiency and cytotoxicity of each complex after prolonged incubation. The 1:2:0.5, 1:2:1 and 1:2:2 ternary complexes showed 158-, 117- and 23-fold photochemical enhancement of the transfection, respectively, with approximately 20% decreases in the cell viability. In contrast, the efficient transfection by the PEI polyplex was accompanied by a remarkable decrease (~85%) in the cell viability. Thus, the PCI-mediated gene delivery can avoid long-term toxicity, which is often induced by the polyplexes based on buffering polycations, because the process toxic to the cell is controlled in a light-responsive manner. Also, the ternary complex with a negative ζ-potential value might hardly interact with the negatively charged cell membranes, leading to reduced cytotoxicity in long-term incubation.

The potential of the ternary complex for *in vivo* PCI-mediated gene delivery was studied by the transfection of a reporter gene (a variant of yellow fluorescent proteins, Venus) to the conjunctival tissue in rat eyes on laser irradiation. In this study, the rat eyes received a subconjunctival injection of the ternary complex (360° circumferential to the cornea), and part of the conjunctiva was then irradiated with a semiconductor laser (689 nm) at 2 h post-injection (Fig. 4a). The pDNA/CP_4/DPc ternary complex with a charge ratio of 1:2:1 achieved significant gene expression only at the laser-irradiated site in the conjunctiva in 8 out of 12 eyes (2 days after irradiation; Fig. 4b,c). Neither the ternary complexes with different compositions (that is, the 1:2:0.5 and 1:2:2 ternary complexes) nor ExGen500, which is one of the most efficient synthetic vectors, showed visible transgene expression. With the passage of time, the number of transfected eyes as well as the fluorescent intensity significantly decreased (Fig. 4c). Fluorescent microscopic observation of a frozen section of the conjunctival tissue revealed that the conjunctival epithelial cells were clearly transfected (Fig. 4d,e). Thus, the transfection only at the laser-irradiated site in the conjunctival tissue was achieved by the PCI-mediated gene delivery using the ternary complex. To our knowledge, this is the first success in PCI-mediated gene delivery *in vivo*.

PCI is a smart concept, which allows the cytoplasmic delivery of macromolecular compounds in a light-inducible

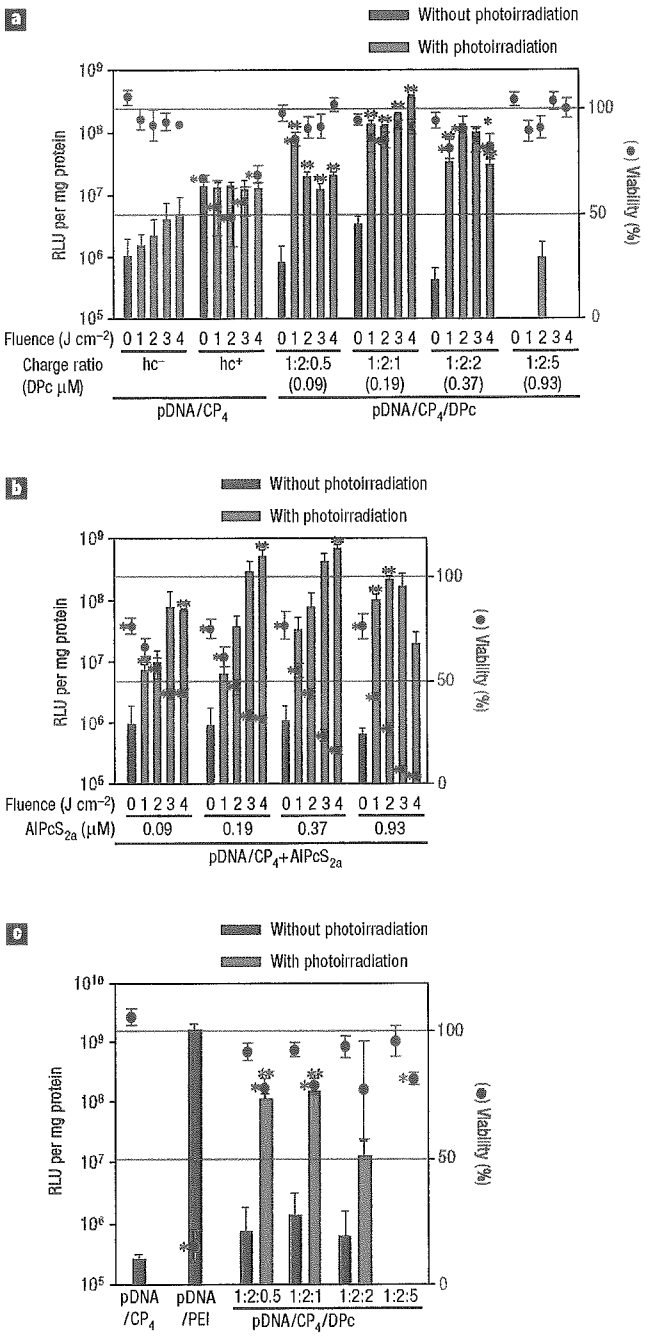

Figure 3 ***In vitro*** **tranfection efficiency and cytotoxicity to HeLa cells. a**, The effect of fluence on the transfection efficiency (bars) and photocytotoxicity (dots) of the pDNA/CP_4 and pDNA/CP_4/DPc complexes. Photoirradiation was performed 6 h after incubation with each complex, followed by 48 h post-incubation in a fresh medium. The hc represents hydroxychloroquine. **b**, The effect of fluence on the transfection efficiency (bars) and photocytotoxicity (dots) of the pDNA/CP_4 complex with different concentrations of $AlPcS_{2a}$. The same experimental conditions as **a** were applied. **c**, The transfection efficiency (bars) and photocytotoxicity (dots) when HeLa cells were irradiated 6 h after incubation with each complex at 3.6 J cm^{-2}, followed by 48 h post-incubation without medium replacement. Results are expressed as mean ± s.d. ($n = 4$). The unpaired t-test was used for statistical analysis, and significant changes in the cell viability (treated to untreated) and the transfection efficiency (photoirradiated to non-photoirradiated) are indicated by asterisks * and **, respectively.

manner. In previous studies, it was demonstrated that $AlPcS_{2a}$ and $TPPS_{2a}$ (meso-tetraphenylporphine with two sulphonate groups on adjacent phenyl rings) were effective in PCI-mediated delivery[8–10]. It is assumed that a hydrophobic moiety in these dissymmetric compounds may provide preferable interaction with cell membranes, whereas they are internalized by endocytosis because of high water solubility. However, such an amphiphilic nature of the compounds should generate interaction with the plasma membrane to some extent, possibly photodamaging the plasma membrane. Meanwhile, such amphiphilic photosensitizers may relocalize to some cytoplasmic organelles such as mitochondria and endoplasmic reticulum during the photoirradiation[11,22,23]. It is known that the plasma membrane and some cytoplasmic organelles might be susceptible to the photocytotoxicity[11]. These effects may be a major cause of the photocytotoxicity of $AlPcS_{2a}$ and $TPPS_{2a}$. These compounds are still useful in PCI; however, reduced photocytotoxicity might be desired before considering further applications of this technology. We assume that the selective photodamage of the endosomal membrane is a key to reduced photocytotoxicity in PCI, motivating us to develop different gene carriers based on the PCI concept.

To design gene carriers based on the PCI concept, the following points should be considered. (i) For *in vivo* applications, the photosensitizing units should be integrated into gene carriers as one component, because separate administration of photosensitizers might result in their diffused localization to the surrounding tissues, which may decrease the efficiency in the PCI-mediated gene delivery and cause the phototoxicity to the surrounding tissues. (ii) Following internalization by the endocytosis, the photosensitizers should be released from gene carriers, otherwise, pDNA could be photochemically inactivated on photoirradiation. (iii) The photosensitizers should have increased affinity for cell membranes under endosomal conditions to accomplish the photochemical rupture of the endosomal membrane. In the ternary complex system, we suggest that DPc may be released from the complex to interact with the endosomal membrane (Fig. 2b), satisfying the aforementioned requirements for effective PCI-mediated gene delivery (Fig. 5).

In *in vitro* experiments, both the ternary complex and the PCI using $AlPcS_{2a}$ showed reduced cell viability as the fluence increased, and the degree of the cytotoxicity depended on the cell lines (Fig. 3a,b, and see Supplementary Information, Figs S1 and S2). Indeed, the PCI conditions have been optimized depending on each cell line[9,10]. However, in this study, a comparison under the same experimental conditions revealed that the ternary complex showed a wider range of safe light doses, in which remarkable enhancement of the transfection was accomplished without reduced cell viability, irrespective of cell lines and incubation time (Fig. 3a and see Supplementary Information, Fig. S2). These results may be due to control of the initial steps in the PCI and highly selective photodamage to the endosomal membrane as described above. We believe that such an expanded range of safe light dose might have resulted in our success in the PCI-mediated gene delivery *in vivo*.

The reduced photocytotoxicity of the ternary complexes might be one of the most important achievements in this study. Because of the pH-dependent membrane binding ability of DPc (Fig. 2b), the photocytotoxicity seems to be reduced when DPc is relocated from the acidic endocytic vesicles into the cytosol. A cytosolic localization of DPc may not be expected to cause phototoxicity owing to low stability of singlet oxygen in aqueous media. Alternatively, it seems that DPc may undergo slower diffusion in the cytosol because of its larger size compared with $AlPcS_{2a}$ and have a reduced chance of relocalizing in susceptible cytoplasmic organelles. However, these assumptions remain to be clarified.

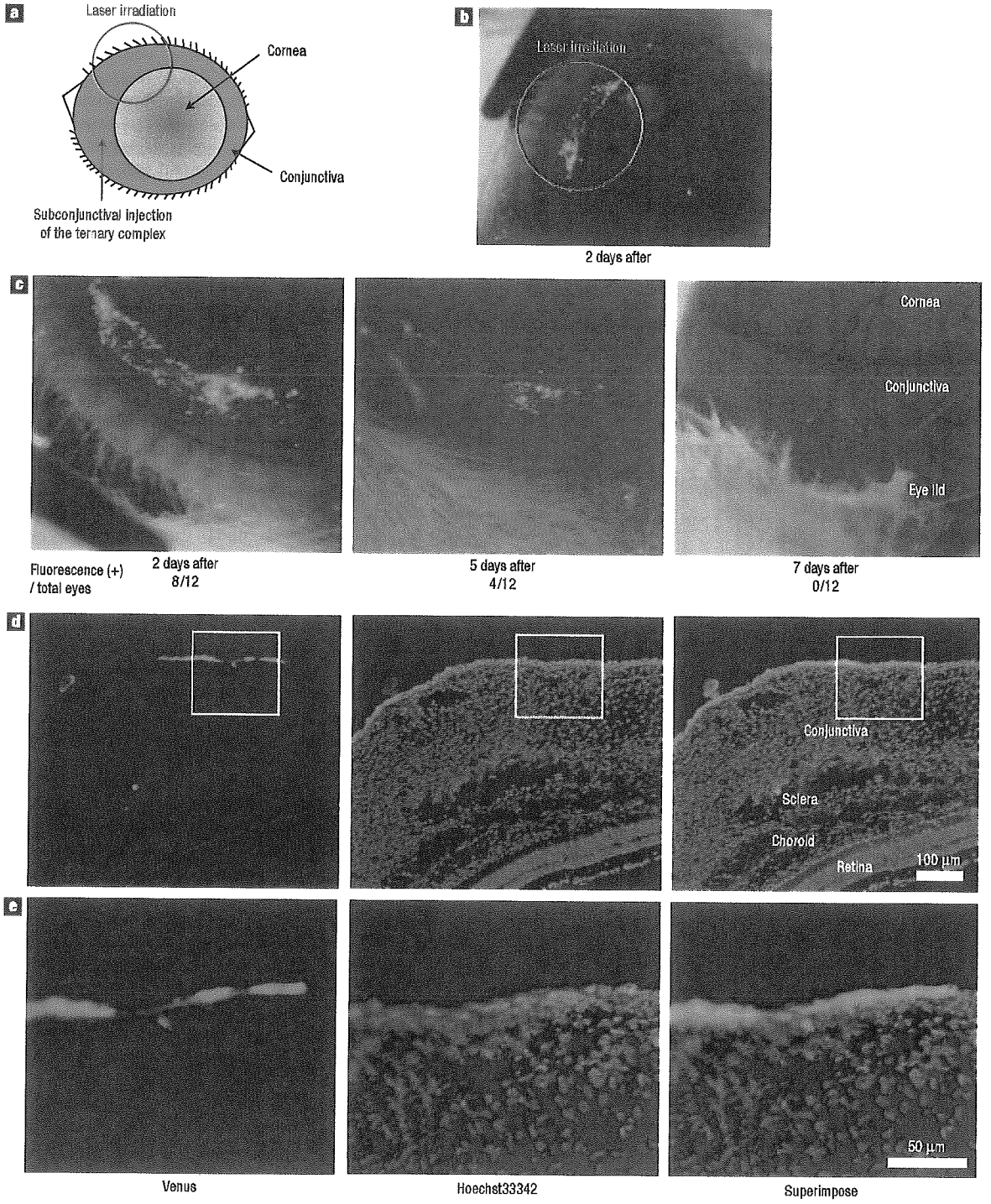

Figure 4 Transfection to the conjunctival tissue to rat eyes. a, The scheme for *in vivo* transfection. Rats were given a subconjunctival injection (coloured in light blue) of each complex containing 15 μg pDNA encoding a variant of a yellow fluorescent protein (Venus). At 2 h post-injection, a part of the conjunctiva (red circle) was irradiated with a light of 689 nm. **b**,**c**, Fluorescent images of the Venus expression in the rat eye at 2, 5 and 7 days after the photochemical transfection using the 1:2:1 ternary complex. The fluorescent-positive eyes/total eyes are indicated below the images. **d**, A fluorescent image of the Venus expression in the frozen section of the conjunctival tissue. The image was taken 2 days after the photochemical transfection using the pDNA/CP_4/DPc 1:2:1 ternary complex. The cell nuclei were stained in blue. **e**, A magnified image of the white square in the above fluorescent image.

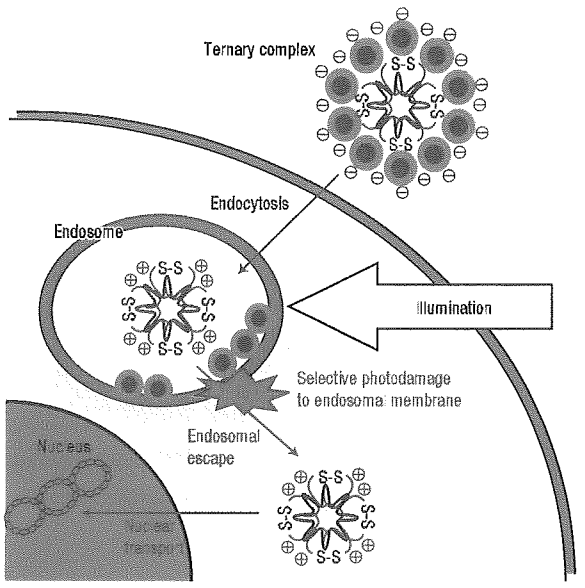

Figure 5 A scheme for itinerary of the ternary complex to the transgene expression. The ternary complex was designed to control the initial steps (that is, internalization by the endocytosis and photodamage of the endosomal membrane to release the polyplex to the cytoplasm) in the PCI-mediated gene delivery.

In the ternary complex system, there is still room for optimization of each component. For example, the polyplex-forming polycations can be optimized, because a variety of polycations can be used for the formation of the ternary complex. Indeed, the ternary complex was formed from poly(L-lysine) at a charge ratio of 1:2:2 (see Supplementary Information, Table S1), and the pDNA/poly(L-lysine)/DPc ternary complex showed approximately 15-fold photochemical enhancement of the transfection with a 50% decrease in the cell viability (see Supplementary Information, Fig. S3). This result suggests that the polyplex-forming polycations significantly affect the transfection efficiency and cytotoxicity, highlighting the importance of optimization of the polycations. In the present study, the CP_4 peptide, of which the nuclear localization and the effective gene transfection following the translocation into the cytoplasm were demonstrated in the previous study[17], was used to prepare the ternary complex, and we successfully obtained the PCI-mediated gene transfection *in vitro* and *in vivo*. Further optimization of the polycations is our future interest, and the studies in this direction will be reported elsewhere.

This system can be potentially useful for the gene therapy of ophthalmic diseases[24]. The molecular design could be expanded to a systemically targeted gene carrier for the treatment of various diseases, including solid tumours. Spatial control of transgene expression in the body will ensure the effectiveness and safety of *in vivo* gene therapy.

METHODS

POLYMER SYNTHESIS AND CHARACTERIZATION

Synthesis of ionic DPc (Fig. 1a) was performed according to the method reported in ref. 25. The detailed synthetic procedure is described in Supplementary Information. The absorption spectra revealed that DPc shows B band absorption at 350 nm and strong Q band absorption at 685 nm.
A cationic peptide $C(YGRKKRRQRRRG)_2$ (CP_2) was synthesized by the Peptide Institute (Osaka, Japan). The CP_4 peptide was prepared by oxidation of the CP_2 peptide in 10 mM of Tris–HCl buffer (pH 7.4) over 14 days. PAA homopolymer (DP: 26; weight-averaged/number-averaged molecular mass (M_w/M_n), 1.2) was synthesized as reported in ref. 26.

PLASMID DNA

A plasmid DNA, pCAcc+Luc, containing a firefly luciferase cDNA driven by a CAG promoter[27] was provided by RIKEN Bioresource Centre (Tsukuba, Japan). Also, a fragment cDNA of SEYFP-F46L (Venus), which is a variant of a yellow fluorescent protein with the mutation F46L[28], was provided by A. Miyawaki of the Brain Science Institute, RIKEN (Wako, Japan), and inserted into the pCAcc vector (pCAcc+Venus). Each plasmid DNA (pDNA) was amplified in competent DH5α *Escherichia coli* and purified by a HiSpeed Plasmid Maxi Kit (Qiagen, Germany). pCAcc+Luc was used for *in vitro* studies, whereas *in vivo* transfection was performed using pCAcc+Venus.

PREPARATION OF THE TERNARY COMPLEX

The pDNA/CP_4 polyplex was prepared by mixing pDNA and CP_4 peptide in 10 mM of Tris–HCl buffer (pH 7.4) at an N/P ratio of 2 (pDNA concentration, 100 μg ml^{-1}). At 30 min after incubation at ambient temperature, the pDNA/CP_4 polyplex solution was mixed with the DPc solution with varying charge molar ratios of pDNA/CP_4/DPc, followed by an extra 30-min incubation at ambient temperature to obtain the pDNA/CP_4/DPc ternary complex. The ternary complexes with varying ratios of DPc were characterized by a gel retardation assay.

CHARACTERIZATION OF THE TERNARY COMPLEX

The size and polydispersity were evaluated by dynamic light scattering measurements using a DLS-7000 instrument (Otsuka Electronics, Osaka, Japan) equipped with an Ar-ion laser (488 nm). The ζ-potential was measured by a laser-Doppler electrophoresis ELS-6000 instrument (Otsuka Electronics) equipped with a He–Ne ion laser (633 nm). AFM imaging was performed in a tapping mode with a standard silicon probe 160 μm in length using an NVB 100 microscope (Olympus, Tokyo, Japan) operated by Nanoscope IIIa software (Digital Instruments, Santa Barbara, California). Detailed experimental conditions are described in the Supplementary Information.

OCTANOL/WATER PARTITIONING

The experimental procedure is described in the Supplementary Information.

FLOW CYTOMETRY ANALYSIS AND CONFOCAL MICROSCOPIC OBSERVATION

The amount of uptake of each polyplex containing pDNA labelled with fluorescein by HeLa cells was analysed by flow cytometry. The detailed experimental conditions are described in the Supplementary Information. Confocal observation of FITC-labelled dextran (M_w: 10,000–15,000) co-incubated with the 1:2:1 ternary complex in HeLa cells before and after photoirradiation was performed using LSM510 (Carl Zeiss, Jena, Germany). Detailed experimental conditions are provided in the Supplementary Information.

IN VITRO TRANSFECTION STUDY

HeLa cells (10,000 cells) on a 24-well culture plate were incubated with each polyplex containing 1 μg pDNA in 0.5 ml of Dulbecco's Modified Eagle's Medium (DMEM) containing 10% fetal bovine serum (FBS), followed by 6- or 24-h incubation and fresh medium replacement. The culture plates were photoirradiated using a 300-W halogen lamp (fluence rate, 3.0 mW cm^{-2}) equipped with a band-pass filter (400–700 nm) with increased fluence (0.9–3.6 J cm^{-2}). After 48 h post-incubation, the transfection efficiency was evaluated by the Luciferase Assay System (Promega, Madison, Wisconsin) and a Lumat LB9507 luminometer (Berthold Technologies, Bad Wildbad, Germany), whereas the cell viability was evaluated by the 3-(4,5-dimethylthiazol-2-yl)-2,5-diphenyltetrazolium bromide (MTT) assay. Sulphonated aluminium phthalocyanine ($AlPcS_{2a}$) and PEI (25 kDa) were purchased from Frontier Scientific (Logan, Utah) and Sigma-Aldrich (St Louis, Missouri), respectively.

IN VIVO TRANSFECTION TO CONJUNCTIVA

Wistar rats (male, 6 weeks old, number of animals $n = 12$; Saitama Experimental Animal Supply, Saitama, Japan) were given a subconjunctival injection of 150 μl of each complex containing 15 μg pDNA (pCAcc+Venus). At 2 h post-injection, the rats were anesthetized and part of the conjunctiva was irradiated using a 689-nm semiconductor laser emitted from laser equipment built in-house (Topcon, Tokyo, Japan) with 2.0 mW laser power and 4 mm projection diameter for 60 s (1 J cm^{-2}). The fluorescent images of the Venus

expression in a rat eye and the conjunctival tissues were taken as described in Supplementary Information. All the experimental procedures were handled in accordance with the guidelines of the Animal Committee of the University of Tokyo. The polyplex from linear PEI, with ExGen500 (Fermentas, Vilnius, Lithuania) as a control vector, was prepared at N/P ratio = 6.

Received 12 July 2005; accepted 28 September 2005; published 20 November 2005.

References

1. Ogris, M. & Wagner, E. Targeting tumors with non-viral gene delivery systems. *Drug Discov. Today* **7**, 479–485 (2002).
2. Taira, K., Kataoka, K. & Niidome, T. (eds) *Non-viral Gene Therapy: Gene Design and Delivery* (Springer, Tokyo, 2005).
3. Merdan, T., Kopecek, J. & Kissel, T. Prospects for cationic polymers in gene and oligonucleotide therapy against cancer. *Adv. Drug Deliv. Rev.* **54**, 715–758 (2002).
4. Salem, A. K., Searson, P. C. & Leong, K. W. Multifunctional nanorods for gene delivery. *Nature Mater.* **2**, 668–671 (2003).
5. Behr, J. P. The proton sponge. A trick to enter cells the viruses did not exploit. *Chimia* **51**, 34–36 (1997).
6. Berg, K. *et al.* Photochemical internalization: a novel technology for delivery of macromolecules into cytosol. *Cancer Res.* **59**, 1180–1183 (1999).
7. Høgset, A., Prasmickaite, L., Tjelle, T. E. & Berg, K. Photochemical transfection: A new technology for light-induced, site-directed gene delivery. *Hum. Gene Ther.* **11**, 869–880 (2000).
8. Prasmickaite, L., Høgset, A. & Berg, K. Evaluation of different photosensitizers for use in photochemical gene transfection. *Photochem. Photobiol.* **73**, 388–395 (2001).
9. Høgset, A. *et al.* Photochemical transfection: A technology for efficient light-directed gene delivery. *Somat. Cell Mol. Genet.* **27**, 97–113 (2002).
10. Høgset, A. *et al.* Photochemical internalization in drug and gene delivery. *Adv. Drug Deliv. Rev.* **56**, 95–115 (2004).
11. Macdonald, I. J. & Dougherty, T. J. Basic principle of photodynamic therapy. *J. Porphyrins Phthalocyanines* **5**, 105–129 (2001).
12. Esfand, R. & Tomalia, D. A. Poly(amidoamine) (PAMAM) dendrimers: from biomimicry to drug delivery and biomedical applications. *Drug Discov. Today* **6**, 427–436 (2001).
13. Gillies, E. R. & Frechet, J. M. Dendrimers and dendritic polymers in drug delivery. *Drug Discov. Today* **10**, 35–43 (2005).
14. Duncan, R. The dawning era of polymer therapeutics. *Nature Rev. Drug Discov.* **2**, 347–360 (2003).
15. Kobayashi, H. *et al.* Lymphatic drainage imaging of breast cancer in mice by micro-magnetic resonance lymphangiography using a nano-size paramagnetic contrast agent. *J. Natl Cancer Inst.* **96**, 703–708 (2004).
16. Tang, M., Redemann, C. T. & Szoka, F. C. Jr. In vitro gene delivery by degraded polyamidoamine dendrimers. *Bioconjugate Chem.* **7**, 703–714 (1996).
17. Rudolph, C. *et al.* Oligomers of the arginine-rich motif of the HIV-1 TAT protein are capable of transferring plasmid DNA into cells. *J. Biol. Chem.* **278**, 11411–11418 (2003).
18. Caruso, F., Caruso, R. A. & Möhwald, H. Nanoengineering of inorganic and hybrid hollow spheres by colloidal templating. *Science* **282**, 1111–1114 (1998).
19. Donath, E. *et al.* Novel hollow polymer shells by collid-templated assembly of polyelectrolytes. *Angew. Chem. Int. Edn* **37**, 2002–2005 (1998).
20. Levitan, H. & Barker, J. L. Salicylate. Structure-activity study of its effects on membrane permeability. *Science* **176**, 1423–1425 (1972).
21. Itaka, K. *et al.* in *Carrier-Based Drug Delivery* (ed. Svenson, S.) 154–159 (ACS Symp. Series Vol. 879, Americal Chemical Society, 2004).
22. Moan, J., Berg, K., Anholt, A. & Madslien, K. Sulfonated aluminum phthalocyanines as sensitizers for photochemotherapy. Effects of small doses on localization, dye fluorescence and photosensitivity in V79 cells. *Int. J. Cancer* **58**, 865–870 (1994).
23. Rodal, G. H., Rodal, S. K., Moan, J. & Berg, K. Liposome-bound Zn(II)-phthalocyanine. Mechanisms for cellular uptake and photosensitization. *J. Photochem. Photobiol. B* **45**, 150–159 (1998).
24. Daiger, S. P. Was the human genome project worth the efforts? *Science* **308**, 362–364 (2005).
25. Ng, A. C. H., Li, X. & Ng, D. K. P. Synthesis and photophysical properties of nonaggregated phthalocyanines bearing dendritic substitutes. *Macromolecules* **32**, 5292–5298 (1999).
26. Harada, A. & Kataoka, K. Formation of polyion complex micelles in aqueous milieu from a pair of oppositely-charged block copolymers with poly(ethylene glycol) segments. *Macromolecules* **28**, 5294–5299 (1995).
27. Niwa, H., Yamamura, K. & Miyazaki, J. Efficient selection for high-expression transfectants with a novel eukaryotic vector. *Gene* **108**, 193–199 (1991).
28. Nagai, T. *et al.* A variant of yellow fluorescent protein with fast and efficient mutation for cell-biological applications. *Nature Biotechnol.* **20**, 87–90 (2002).

Acknowledgements

We thank N. Kanayama (the University of Tokyo), S. Kawauchi (National Defense Medical College) and K. Date (the University of Tokyo) for technical assistance. This work was supported in part by the Core Research Program for Evolutional Science and Technology (CREST) from Japan Science and Technology Agency (JST).

Correspondence and requests for materials should be addressed to K.K.[3]

Supplementary Information accompanies this paper on www.nature.com/naturematerials.

Competing financial interests

The authors declare that they have no competing financial interests.

OsteoArthritis and Cartilage (2005) **13**, 632–641

doi:10.1016/j.joca.2005.03.004

Osteoarthritis and Cartilage

International Cartilage Repair Society

OARSI OSTEOARTHRITIS RESEARCH SOCIETY INTERNATIONAL

Osteoarthritis development in novel experimental mouse models induced by knee joint instability

S. Kamekura M.D.†, K. Hoshi M.D., Ph.D.‡, T. Shimoaka M.D., Ph.D.†, U. Chung M.D., Ph.D.‡, H. Chikuda M.D., Ph.D.‡, T. Yamada M.D., Ph.D.†, M. Uchida Ph.D.§, N. Ogata M.D.†, A. Seichi M.D., Ph.D.†, K. Nakamura M.D., Ph.D.† and H. Kawaguchi M.D., Ph.D.†*

† *Department of Orthopaedic Surgery, University of Tokyo, Tokyo, Japan*

‡ *Department of Tissue Engineering, Faculty of Medicine, University of Tokyo, Tokyo, Japan*

§ *Biomedical Research Laboratory, Kureha Chemical Industry Co., Ltd., Tokyo, Japan*

Summary

Objective: Although osteoarthritis (OA) is induced by accumulated mechanical stress to joints, little is known about the underlying molecular mechanism. To apply approaches from mouse genomics, this study created experimental mouse OA models by producing instability in the knee joints.

Methods: The models were of four types: severe, moderate, mild, and medial, depending on the severity and direction of instability imposed by combinations of ligament transection and menisectomy. OA development was evaluated by X-ray and histology by Safranin-O staining, and quantified using our original gradings. Expressions of type II, IX and X collagens and matrix metalloproteinase (MMP)-2, -3, -9 and -13 were further examined by immunohistochemistry and in situ hybridization (ISH).

Results: The severe, moderate and mild models exhibited OA development in the posterior tibial cartilage. The severe model showed cartilage destruction at 2 weeks and osteophyte formation at 4–8 weeks after surgery; however, the mild model showed only a partial cartilage destruction at 8 weeks. The grading confirmed that the OA disorders progressed depending on the severity of joint instability. In the medial model, the OA development in the medial tibial cartilage was similar to that in the posterior cartilage of the mild model. Among the collagens and MMPs, type X collagen and MMP-13 were markedly induced and colocalized in the early stage OA cartilage.

Conclusion: We established four types of mouse models exhibiting various speeds of OA progression. By applying a mouse genomics approach to the models, molecular backgrounds in various stages of OA development can be clarified.

Key words: Osteoarthritis, Mechanical stress, Mouse, Chondrocyte, Hypertrophy, MMP-13.

Introduction

Osteoarthritis (OA), a chronic degenerative joint disorder characterized by articular cartilage destruction and osteophyte formation, is prevalent in society as a major cause of disability. In Western countries, 10–50% of the senior population is affected by OA, a quarter of whom are severely disabled due to joint symptoms[1,2]. In Japan as well, approximately 10 million of the country's 120 million inhabitants are suffering from OA, with the figure increasing by nine hundred thousands every year. Because of the prevalence of the disease in the elderly, this trend is occurring worldwide as a consequence of increasing longevity due to the overall improvement in living conditions and health status[3]. Despite significant social demand, research on OA is still marginalized within biomedical research, so that the cellular and molecular bases for the disease are largely unmapped. Risk factors of OA so far identified by previous epidemiologic studies are limited to age, trauma history, occupation and gender[4]. Since these factors are closely related to the mechanical loading to the joints, it is assumed that a large part of OA is induced by accumulated mechanical stress. In efforts to clarify the mechanisms by which the stress lead to OA development, animal models of OA induced by producing instability of joints through surgical intervention have been developed in dogs, rabbits, guinea pigs and rats[5–8].

Due to rapid progress of mouse genomics and the availability of transgenic and knockout mice, the mouse is now the most ideal animal model for the study of molecular backgrounds of physiological and pathological conditions. There are actually several mouse OA models: spontaneous models exhibiting OA with aging such as STR/ort mouse[9] and C57 black mice[10], and gene-manipulated mice such as Del1[11]. However, since most of these models exhibit other cartilage disorders such as chondrodysplasia due to genetic mutations of cartilage matrix components, etc. even in the absence of mechanical stress, they are inadequate to study the mechanism of the stress-induced OA. Based on the hypothesis that the difficulty in elucidation of the OA mechanism is at least partly because the stress-induced OA animal

*Address correspondence and reprint requests to: Hiroshi Kawaguchi, Department of Orthopaedic Surgery, Faculty of Medicine, University of Tokyo, Hongo 7-3-1, Bunkyo, Tokyo 113-8655, Japan. Tel: 81-3-3815-5411x33376; Fax: 81-3-3818-4082; E-mail: kawaguchi-ort@h.u-tokyo.ac.jp

Received 10 August 2004; revision accepted 2 March 2005.

models have been confined to larger animals for which no gene manipulation technique has yet been developed, the present study aimed at creating stress-induced OA models in mice, that are reproducible and resemble the human OA, using a microsurgical technique to produce instability in the knee joints. The models were of four types: severe, moderate, mild, and medial, depending on the severity and direction of joint instability imposed by combinations of ligament transection and menisectomy. By combining these models, we performed histological analyses of the OA articular cartilage, and looked at the cellular and molecular changes in the development of OA.

Methods

EXPERIMENTAL ANIMALS AND SURGICAL PROCEDURES

All experiments were performed according to the protocol approved by the Animal Care and Use Committee of the University of Tokyo. C57Black6/J mice (18–22 g) were obtained from Charles River Japan Co. (Yokohama, Japan). Mice at 8 weeks of age were divided into three groups: severe, moderate, and mild models ($n = 30$/model). Under general anesthesia with pentobarbiturate (0.5 mg/10 g body weight, i.p., Sigma, St. Louis, Missouri), the bilateral hind limbs were shaved and prepared for aseptic surgery. Figure 1 summarizes the combinations of ligament transection and menisectomy in the mouse knee joints for the four models. In the severe model, the right knee joint was exposed and the patellar ligament (PL) was transected. Then, the anterior/posterior cruciate ligaments (ACL/PCL) and the medial/lateral collateral ligaments (MCL/LCL) were transected, and the medial/lateral menisci (MM/LM) were removed using a surgical microscope and microsurgical technique. After irrigation with saline to remove tissue debris, the skin incision was closed. During the procedure, close attention was paid not to injure the articular cartilage. The contralateral knee joint was sham-operated through the same approach without any ligament transection or menisectomy. The animals were allowed unrestricted activity, food, and water *ad libitum*. In the moderate model, the knee joint was exposed following a medial capsular incision and gentle lateral displacement of the extensor mechanism without transection of the PL. The ACL was transected and the MM was removed. After replacement of the extensor mechanism, the medial capsular incision was sutured and the skin was closed. In the mild model, using the same surgical approach as the moderate model, only ACL was transected and the incision was closed. The medial model was created without ACL transection; for this model the MCL was transected and the MM was removed through the same procedure ($n = 30$).

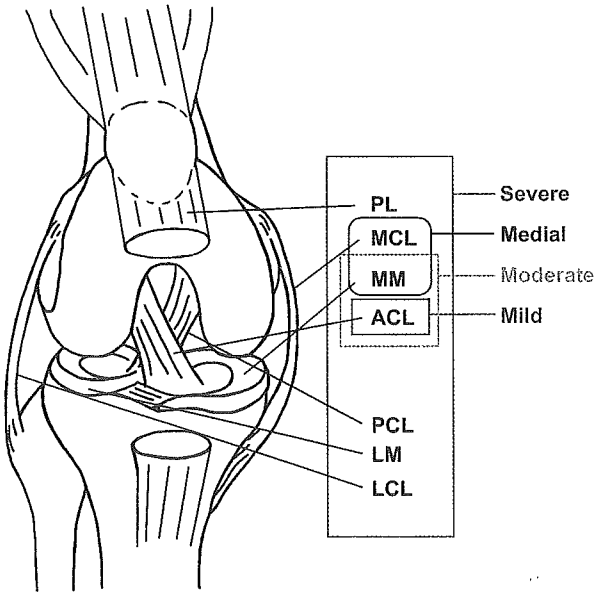

Fig. 1. Scheme of the mouse knee joint and the combinations of ligament transection and menisectomy in the severe, moderate, mild and medial models. PL, patellar ligament; MM, medial meniscus; LM, lateral meniscus; MCL, medial collateral ligament; LCL, lateral collateral ligament; ACL, anterior cruciate ligament; PCL, posterior cruciate ligament.

RADIOLOGICAL AND HISTOLOGICAL ANALYSES

Radiographs of the mouse knee joints were taken in the anteroposterior and lateral projections at 0 (immediately after surgery), 2, 4, and 8 weeks after surgery under general anesthesia using a soft X-ray apparatus (CMB-2; Softex Co., Tokyo, Japan), and were evaluated by a single observer who was blinded with regard to the experimental group. Mice of severe, moderate and mild models were sacrificed at 2, 4, and 8 weeks ($n = 10$ at each time point), and those of the medial model were sacrificed at 2, 4, 8 ($n = 7$ at each time point) and 12 weeks ($n = 9$). The numbers of mice were confirmed to be enough to perform statistical analyses[12]. The whole knee joints were dissected, and fixed in 4% paraformaldehyde (PFA) buffered with phosphate buffered saline (PBS) (pH 7.4) for 4 h at 4°C. The specimens were decalcified for 2 weeks with 10% ethylene-diamine tetraacetic acid (EDTA) (pH 7.4) at 4°C. After dehydration with an increasing concentration of ethanol and embedding in paraffin, 4 μm sagittal sections for the severe, moderate and mild models were cut from the whole medial compartment of the joints, and frontal sections for the medial model were cut from the whole joints. Sections were stained with Safranin-O-fast green, and the OA development in the tibial plateau was quantified by our original histological grading scores of 0–4 for cartilage destruction and 0–3 for osteophyte formation (Table I). The grade of OA was determined as the most advanced grade in all sections by a single observer who was blinded with regard to the experimental group. In an effort to control the inherent subjectivity of the assessment technique, all sections were graded by the same observer on two separate occasions, more than a month apart. Although the intraobserver reproducibility was confirmed to be more

Table I
Histological grading for osteoarthritic changes in mouse model

	Grade
I. Cartilage destruction	
A. No apparent changes	0
B. Loss of superficial zone in articular cartilage	1
C. Defects limited above tidemark	2
D. Defects extending to calcified cartilage	3
E. Exposure of subchondral bone	4
II. Osteophyte formation	
A. None	0
B. Formation of cartilage-like tissues	1
C. Increase of cartilaginous matrix	2
D. Endochondral ossification	3

than 90%, the mean value of the two scorings was defined as the final grade.

IMMUNOHISTOCHEMISTRY

Immunohistochemical localizations of type II, IX and X collagens, matrix metalloproteinase (MMP)-2, -3, -9 and -13 were performed in dewaxed paraffin sections as previously described[13]. The sections were treated with 0.3% hydrogen peroxide in PBS for 30 min at room temperature. To enhance the permeability of the extracellular matrix, glycosaminoglycans were removed by incubating the sections with 2.5% hyaluronidase (Sigma, St. Louis, Missouri) for 30 min at 37°C, as previously reported[14]. After blocking by PBS containing 1% bovine serum albumin (Sigma) for 1 h at room temperature, they were incubated with polyclonal rabbit antibodies against rat type II, IX and X collagens (LSL, Tokyo), and polyclonal goat antibodies against rabbit MMP-2, -3, -9 and -13 (CHEMICON International, Inc., Temecula, CA) at a dilution of 1:100 for 24 h at 4°C. As negative controls, we used non-immune rabbit or goat IgG of the same dilution instead of the primary antibodies. The sections were rinsed in PBS and incubated with the horseradish peroxidase (HRP)-conjugated goat antibodies against rabbit IgG (ICN Biomedicals, Inc., Aurora, Ohio) for 20 min at room temperature. The sections were washed with PBS, immersed in a diaminobenzidine solution for 10 min at room temperature to visualize any immunoreactivity, and were then counterstained with methylgreen.

IN SITU HYBRIDIZATION

In situ hybridization (ISH) with non-radioactive or radioactive probes was performed as previously described with minor modifications[15]. In brief, dewaxed paraffin sections were postfixed with 4% PFA buffered with PBS (PFA–PBS) for 15 min at room temperature. After washing with PBS, sections were digested with 10 μg/ml proteinase K for 15 min in PBS, treated again with 4% PFA–PBS for 10 min to inactivate proteinase K, washed with PBS, incubated with 0.2 N HCl for 10 min, washed with PBS, acetylated with 0.3% acetic anhydride in the presence of 0.1 M triethanolamine for 10 min, treated with 3% hydrogen peroxide/methanol for 30 min, dehydrated with increasing concentrations of ethanol, and air dried. Hybridization with complementary digoxigenin (DIG)-labeled or ^{35}S-labeled riboprobes for mouse *type X collagen* (generously given by B. Olsen, Harvard Medical School, Boston, MA) and mouse *MMP-13* (generously given by S. Schipani, Massachusetts General Hospital, Boston) was performed in a humidified chamber in a solution containing 50% formamide, 10% dextran sulfate, 1× Denhardt's solution, 600 mM NaCl, 10 mM dithiothreitol, 0.25% sodium dodecyl sulfate, and 150 μg/ml transfer RNA for 16 h at 52°C. After hybridization, sections were sequentially washed once with 50% formamide/2× saline sodium citrate (SSC) for 5 min at 52°C, twice with 2× SSC for 1 min at room temperature, once with 10 μg/ml RNaseA/2× SSC for 30 min at 37°C, twice with 2× SSC for 1 min at room temperature, and once with 50% formamide/2× SSC for 5 min at 52°C. For the detection of DIG-labeled probes, slides were blocked by PBS containing 1% bovine serum albumin (Sigma) for 10 min at room temperature, and incubated with HRP-conjugated anti-DIG rabbit polyclonal antibody (Dakopatts, Glostrup, Denmark) at a dilution of 1:100 for 24 h at 4°C. After washing three times with tris-buffered saline containing 0.1% Tween-20 (TBS-T), the sections were immersed in a diaminobenzidine solution for 10 min at room temperature to visualize immunoreactivity, then were counterstained with methylgreen. For the detection of radioactive probes, slides were placed on X-ray films, and the autoradiographs were obtained after overnight exposure. Slides were dipped into NTB-2 (Eastman Kodak, New Haven, CT) and stored at 4°C for the times estimated from the intensity of signals on the X-ray film. After development, sections were counterstained with hematoxylin–eosin.

STATISTICAL ANALYSIS

Means of groups were compared by ANOVA and significance of differences was determined by *post-hoc* testing with Bonferroni's method.

Results

TIME COURSE OF RADIOLOGICAL CHANGES IN THE SEVERE, MODERATE AND MILD MODELS

We first performed radiological analyses of the knee joints in the severe, moderate and mild models (Fig. 2). All mice in the three models exhibited anterior subluxation of the tibiae causing joint destruction and osteophyte formation at the posterior part of the joints. The progression speed of the radiological disorders was dependent upon the severity of joint instability induced by the surgery. The severe model showed joint destruction at 2 weeks and osteophyte formation at the posterior tibiae 4 weeks after surgery. The moderate model showed joint destruction and osteophyte formation at 4 weeks, both of which progressed thereafter. Contrarily in the mild model these changes could not be detected until 8 weeks, although the deterioration of joint congruency and the subchondral sclerotic changes were visible at 8 weeks.

TIME COURSE OF HISTOLOGICAL CHANGES IN THE SEVERE, MODERATE AND MILD MODELS

Histological examinations were then made using Safranin-O staining to learn more of the time course of OA development. In the sham-operated knee joints of the contralateral side, the articular cartilage of the tibiae had a smooth surface, evenly stained with Safranin-O, and attached to the subchondral bone 8 weeks after surgery [Fig. 3(A)]. In the superficial zone of the tibial articular cartilage, one or two layers of flat cells were arranged tangentially, and round cells were observed in the middle zone above the tidemark. These histological findings were similar to those of normal knee cartilage of mice without any surgical intervention at the same age.

Figure 3(B) shows low (left panel) and high (right panel) magnifications of joints, which principally demonstrate the osteophyte formation and cartilage destruction, respectively, at the posterior tibiae in severe, moderate and mild models. In the low magnification feature of the severe model, a cartilaginous tissue extended from the posterior tibial cartilage 2 weeks after surgery, and gradually grew with an increase of the Safranin-O staining at 4 weeks. By 8 weeks, the tissue had developed into an osteophyte through endochondral ossification. In the moderate model, the maturation and development of osteophyte were somewhat slower, corresponding to the radiological findings. Contrarily, osteophyte formation was hardly visible in the mild model until 8 weeks. In these three models,

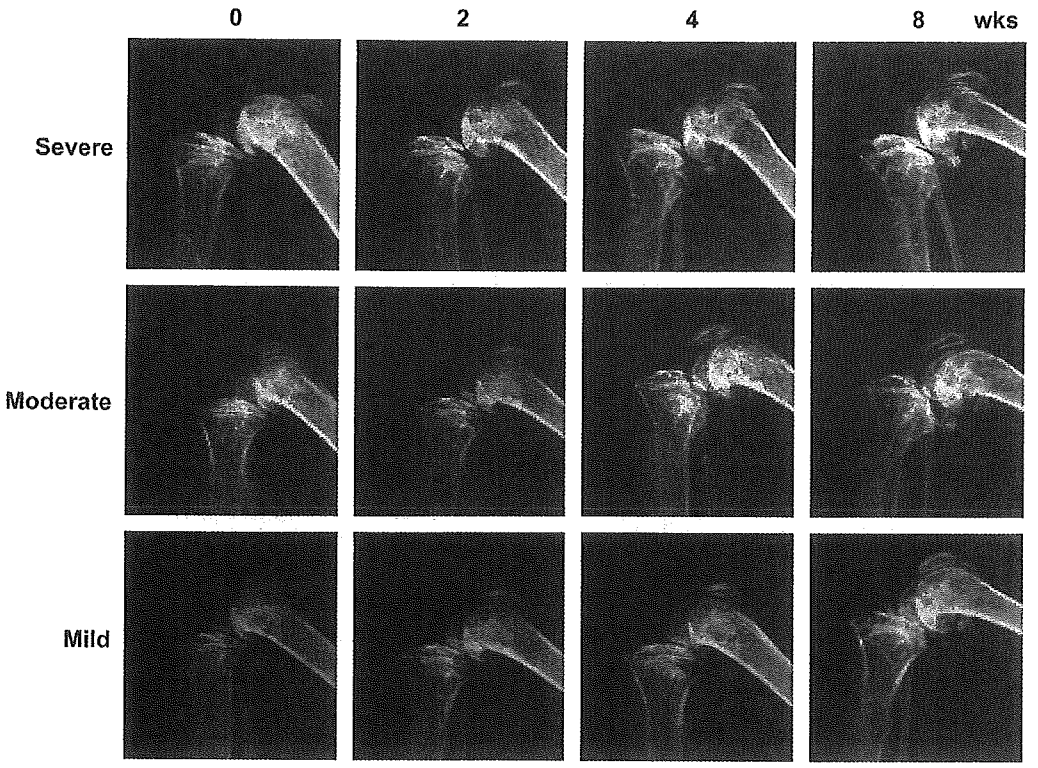

Fig. 2. Time course of lateral X-ray features of the knee joints in the severe, moderate and mild models. Radiographs were taken at the indicated weeks after surgery under general anesthesia using a soft X-ray apparatus. Due to the anterior subluxation of the tibiae, joint destruction and osteophyte formation were visible in the posterior tibial plateau. The changes were dependent on the time after surgery and the severity of joint instability.

thickened synovium due to inflammatory reaction to the surgical invasion was visible at 2 weeks, but not thereafter.

The cartilage destruction at the tibiae seen in the high magnification features of the severe model showed a loss of the superficial zone, a decrease in Safranin-O staining and an increase in cellularity in the middle zone at 2 weeks. At 4 weeks, the defect of the articular cartilage had developed into the calcified cartilage layer below the tidemark, and finally almost the full thickness of the articular cartilage was destroyed by 8 weeks. In the moderate model, the early stage disorders were also noted within 2 weeks, while the defect of articular cartilage was limited to the area above the tidemark at 4 weeks, and gradually extended to the calcified cartilage at 8 weeks. The mild model did not exhibit any changes in the articular cartilage at 2 weeks, but proliferation and shape change of chondrocytes began by 4 weeks. Cartilage destruction in the mild model rarely reached the middle layer even at 8 weeks.

In order to quantify the time course of OA development in the three models, we used our original gradings for cartilage destruction and osteophyte formation (Table I). For the grading of the cartilage destruction, we referred to the simple scoring systems in mouse OA models by Wilhelmi and Faust[10], Helminen *et al.*[16], Chambers *et al.*[17], Saamanen *et al.*[11], and Price *et al.*[18], and modified them, because the mouse cartilage contains only a few cell layers. In addition, osteophyte formation was graded into four ranks, according to the process of endochondral ossification. Based on the histological grading scores, both cartilage destruction and osteophyte formation increased as functions of time after surgery and severity of joint instability (Fig. 4). The severe model exhibited the most drastic increases of both parameters, while the moderate model showed somewhat lower scores, although not significantly different from the severe model. The scores of the mild model were the lowest and remained less than half those of the other two models throughout the observation period up to 8 weeks.

TIME COURSE OF HISTOLOGICAL CHANGES IN THE MEDIAL MODEL

Since the three models above include the ACL transection, they exhibited the anterior subluxation causing the OA development at the posterior part of the joints. Considering that most of the clinical knee OA cases have major disorders in the medial tibial cartilage, we performed transection of the MCL instead of the ACL. Although the MCL transection alone did not lead to any OA changes until 12 weeks after surgery (data not shown), the combination of MCL transection and medial menisectomy caused the cartilage destruction and osteophyte formation in the medial tibial cartilage (Fig. 5). The time course of OA development was similar to or slightly more severe than that of the mild model: proliferation and shape change of chondrocytes at 2–4 weeks, cartilage destruction into the middle zone at 8 weeks, and osteophyte formation at 12 weeks.

COLLAGEN AND MMP EXPRESSION IN THE MOUSE OA MODELS

Cellular changes in the early stage of OA cartilage were determined by immunohistochemistry and ISH for collagens and MMPs, both of which have been implicated in OA

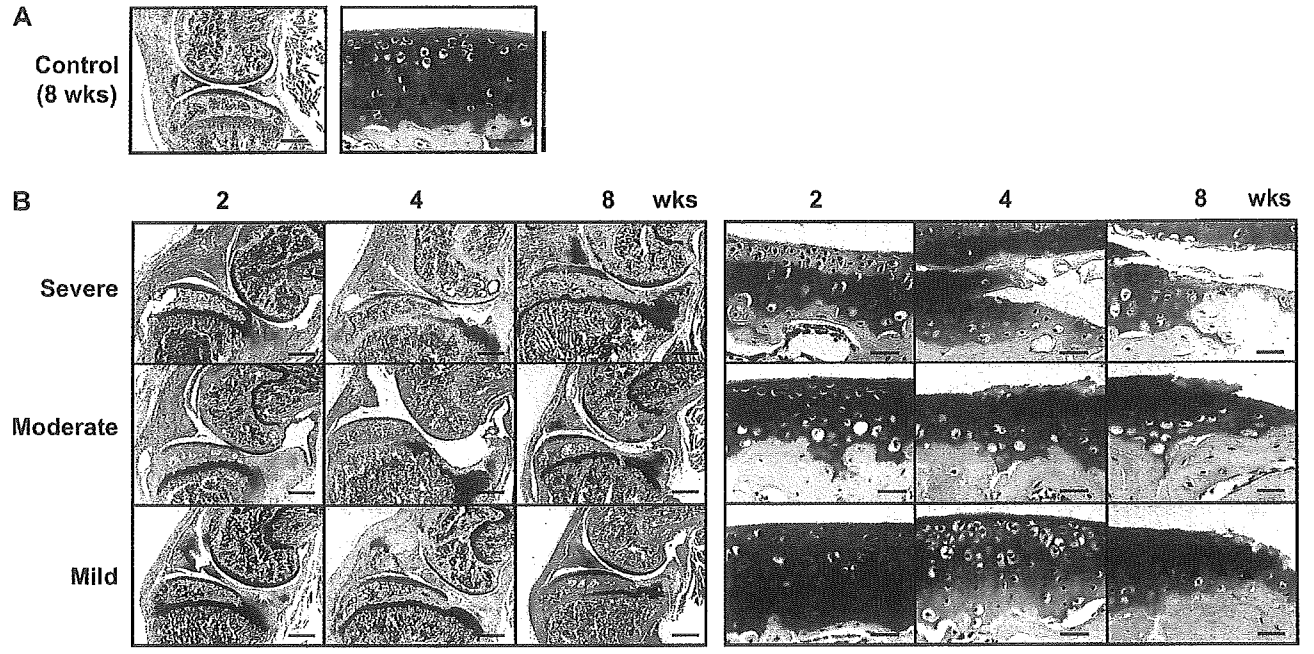

Fig. 3. Time course of histology of the knee joints in the severe, moderate and mild models. After fixation, decalcification and embedding, 4 μm sagittal sections were cut from the whole knee joints, and were stained with Safranin-O-fast green. Arrowheads indicate the level of the tide mark. Scale bar, 1 mm and 50 μm for low and high magnifications, respectively. (A) Low (left) and high (right) magnifications of sham-operated knee joints 8 weeks after surgery. Blue, red, green, and black bars indicate superficial zone, middle/deep zones, calcified cartilage, and subchondral bone, respectively. (B) Low (left) and high (right) magnifications of severe, moderate and mild models at the indicated weeks after surgery, which represent osteophyte formation and cartilage destruction, respectively.

development. The immunohistochemical localization of cartilage specific type II and IX collagens was comparable between the OA cartilage in the moderate model and the sham-operated control 2 weeks after surgery [Fig. 6(A)]. In both mice, type II collagen was strongly stained in all zones of the articular cartilage both above and below the tidemark, while type IX collagen was mainly localized in and around chondrocytes in the superficial and middle zones of cartilage above the tidemark, but weakly in the calcified cartilage below the tidemark. Type X collagen, a specific marker of hypertrophic chondrocytes, was faintly stained in the calcified cartilage below the tidemark; however, the OA cartilage showed its immunoreactivity in and around chondrocytes above the tidemark. ISH confirmed the expression of mRNA in chondrocytes of these areas, indicating the presence of pathological chondrocytes that undergo hypertrophic differentiation in the early stage of OA development [Fig. 6(B)]. In the severe, mild, and medial models, type X collagen expression in chondrocytes of the superficial and middle zones was also seen at 1, 4, and 4 weeks, respectively, after surgery (data not shown).

We next compared MMP-2, -3, -9 and -13 expression between the OA cartilage in the moderate model and the sham-operated control 2 weeks after surgery [Fig. 7(A)].

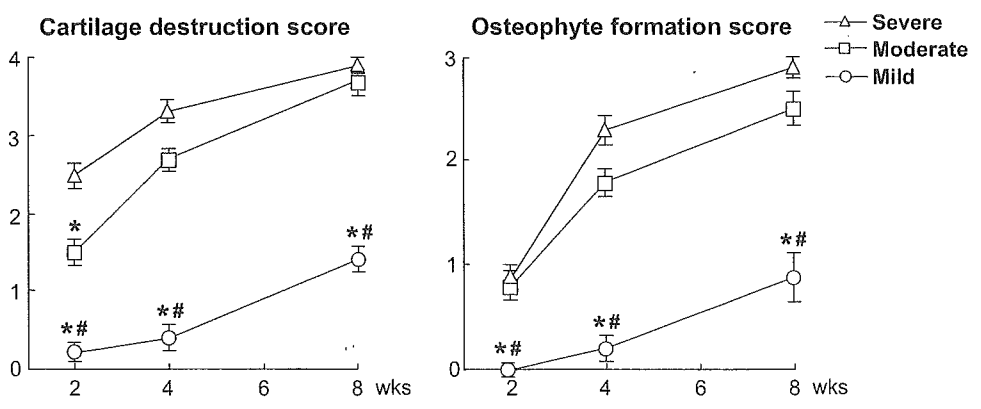

Fig. 4. Time course of OA development by the histological grading scores in the severe, moderate and mild models. The OA development was graded by scores of 0–4 for cartilage destruction and 0–3 for osteophyte formation as shown in Table I. Both cartilage destruction and osteophyte formation scores increased as functions of time after surgery and severity of joint instability. Data are expressed as the means (symbols) ± S.E.M. (error bars) for 10 mice/time point in each model. *$P < 0.01$ vs severe model, #$P < 0.01$ vs moderate model.

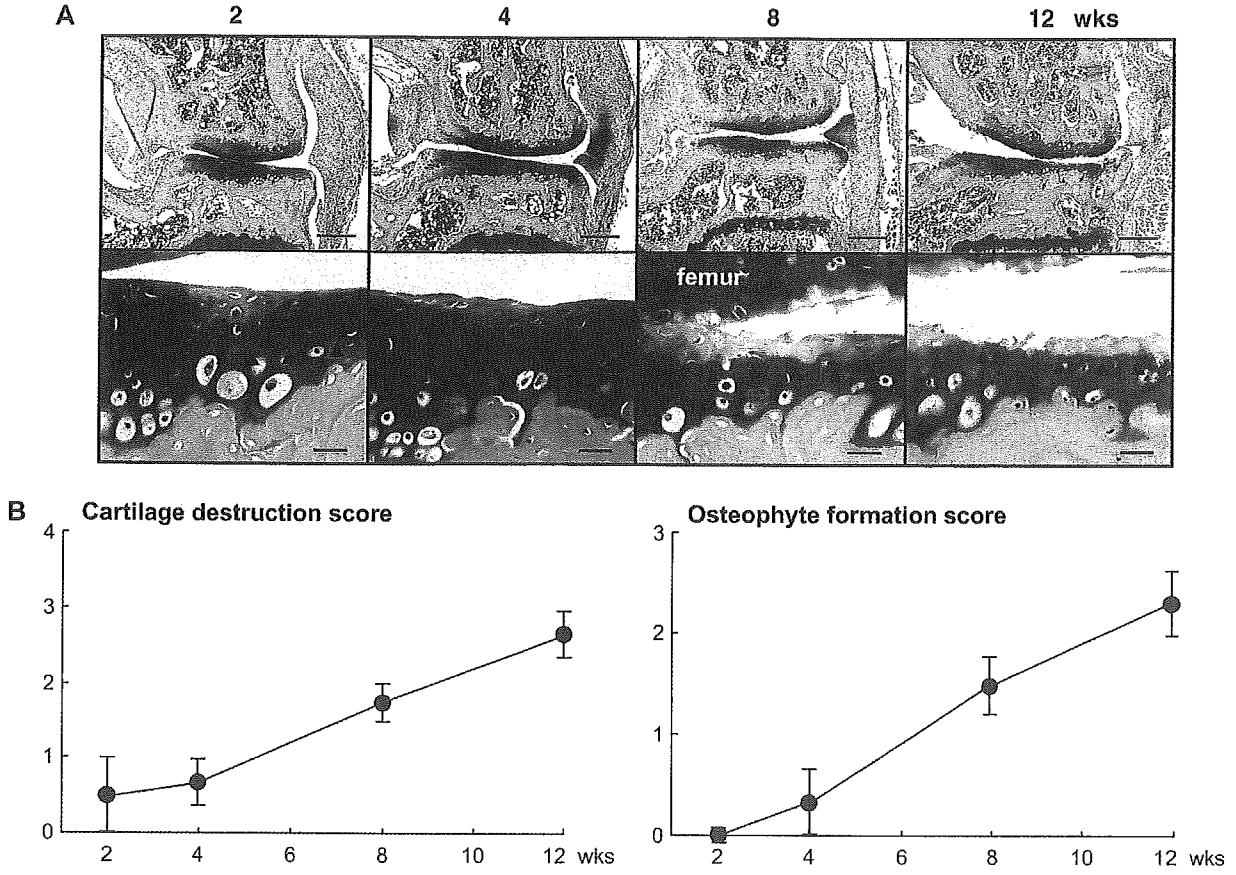

Fig. 5. Time course of OA development in the medial model. After fixation, decalcification and embedding, 4 μm frontal sections were cut from the whole knee joints, and were stained with Safranin-O-fast green. (A) Histological features of low (top) and high (bottom) magnifications at the indicated weeks after surgery. Arrowheads indicate the level of the tide mark. Scale bar, 500 μm and 50 μm for low and high magnifications, respectively. (B) Time course of OA development by the histological grading as shown in Table I. Data are expressed as the means (symbols) ± S.E.M. (error bars) for seven mice at 2, 4, 6 weeks and for nine mice at 12 weeks.

MMP-2 and MMP-9 were localized solely in the calcified cartilage and subchondral bone area, while MMP-3 immunolocalization was visible above the tidemark. These localizations were similar in the OA and control cartilages. In contrast, the immunostaining of MMP-13 was enhanced in the superficial and middle zones of the OA cartilage, which was rarely seen in the control. Since the localization of MMP-13 was quite similar to that of type X collagen shown in Fig. 6(A), we assume that MMP-13 is produced by pathological hypertrophic chondrocytes in early OA cartilage.

To examine the expression patterns of type X collagen and MMP-13 in more advanced OA cartilage, immunostaining was performed in the severe model 4 weeks after surgery. These were also colocalized in the areas adjacent to the destructive lesion of the OA cartilage, confirming the close connection between the hypertrophic differentiation and MMP-13 production by chondrocytes [Fig. 7(B), top]. When ISH analyses of type X collagen and MMP-13 in the growth plate of fetal mouse tibiae (E17.5) were performed to examine their connection under physiological conditions, they were not colocalized as in OA cartilage: only the highly differentiated cells in the type X collagen-positive chondrocytes expressed MMP-13. These results suggest that the appearance of abnormal chondrocytes that simultaneously undergo hypertrophic differentiation and MMP-13 expression in the superficial and middle zones is characteristic in the development of OA.

Discussion

As a first step in applying mouse genomics that has recently made a breakthrough in the biological research on OA development, the present study established four types of experimental mouse OA models by producing instability in the knee joints. Although it may seem difficult to perform the operation in the small joints of mice without direct damage at the time of surgery, microscopic and microsurgical technique have made it much safer and easier. In fact, a beginner performing the operation for the first time who has at least experience in clinical surgery under a microscope can accomplish the entire procedure within 20 min without damaging the articular cartilage.

The early stage changes in the mouse articular cartilage after surgery were found to be a defect of the superficial zone and a decrease of Safranin-O staining, followed by progressing cartilage destruction and aggravation of joint congruency that created a vicious circle to advance the condition. These changes were identical to the human OA pathology reported as arthroscopic and histological findings[19,20]. Along with the catabolic changes, anabolic reactions such as chondrocyte proliferation, subchondral sclerosis, and osteophyte formation were also seen in the human OA cartilage. Although previous OA models of larger animals are known to recapitulate these anabolic changes[7], it was difficult to accurately evaluate and quantify the

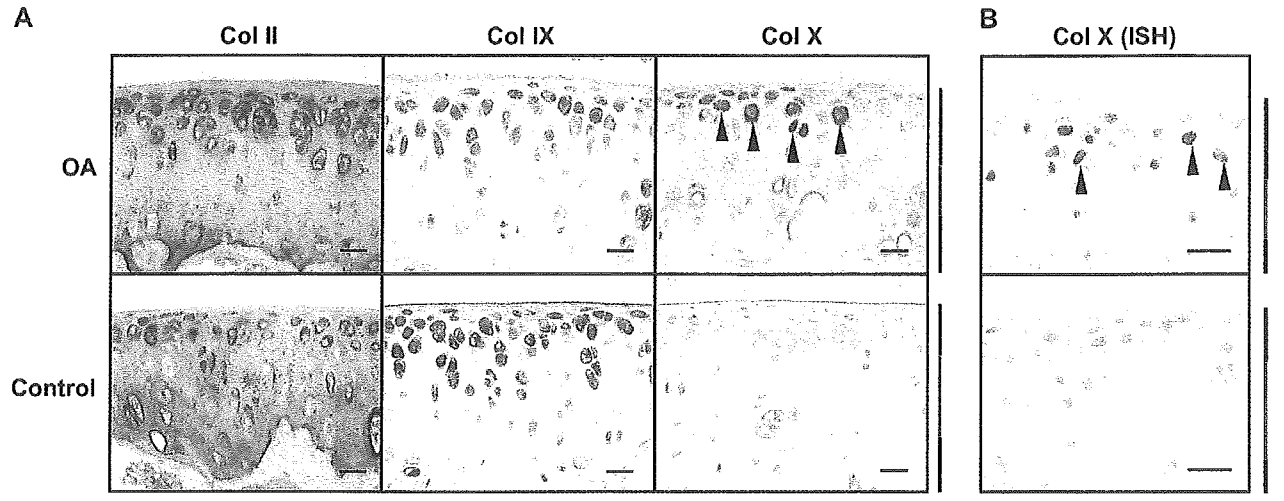

Fig. 6. Immunohistochemistry for type II, IX and X collagens (Col II, Col IX and Col X) (A) and ISH for Col X mRNA (B) in the OA and control cartilages. Stainings of the OA cartilage in the moderate model and the sham-operated control 2 weeks after surgery. Blue, red, green, and black bars indicate superficial zone, middle/deep zones, calcified cartilage, and subchondral bone, respectively. Scale bar, 50 μm. Immunohistochemistry was performed in dewaxed paraffin sections with polyclonal rabbit antibodies against rat Col II, Col IX and Col X as described in Methods. ISH was performed in the paraffin sections using complementary DIG-labeled riboprobes for mouse Col X. The sections were counterstained with methylgreen. Although Col II and Col IX expressions were similar between the OA and control cartilages, Col X was localized in the chondrocytes of the superficial and middle zones (arrowheads) of the OA cartilage, but not of the control.

chondrocyte proliferation and subchondral bone sclerosis in the current mouse models in which the articular cartilage contains only a few cell layers. We therefore did not include the anabolic parameters except the osteophyte formation in the present histological grading system, and created a simpler system than Mankin's grading system[21] that is frequently used for OA of larger animals and humans.

Although the instability was present in the knee joints, the OA change was much more severe in the tibial cartilage than in the femoral condyle cartilage. Since the cartilage layer is much thinner and osteophyte formation is rarely seen in the femoral condyle, it is difficult to quantify OA development with the same accuracy as in the tibial cartilage. Hence, the current models focused on OA change in the tibial cartilage. In the three models with ACL transection, severe, moderate and mild, OA development in the posterior tibial cartilage was dependent on the severity of joint instability, indicating that combinations of these models will enable us to identify the molecular backgrounds at various stages. The severe and moderate models appeared to be useful to evaluate reactive osseous changes like osteophyte formation which is characteristic in the late stage of OA. Because the moderate model showed somewhat slower progress in the early stage of cartilage destruction than the severe model, this model also seemed suitable to follow the entire process including the early stage changes. The OA development in the mild model was limited to a partial cartilage destruction, and chondrocyte morphology was relatively preserved during the observation period, indicating that this model is useful for detailed investigations of the early stage.

There is a recent report using a mouse OA model through MCL transection and partial medial menisectomy of the knee joints[22]. In that study, Clements *et al.* observed OA development in mice lacking interleukin-1β (IL-1β), IL-1β-converting enzyme, stromelysin 1 or inducible nitric oxide synthase, all of which were theoretically thought to play important roles in the development of the condition[23]. However, all mutant mice unexpectedly exhibited an acceleration of cartilage destruction 4 weeks after surgery, implying that these factors were essential for balancing anabolism and catabolism in the early stage of OA development, as the authors discussed. The Clements model resembles the medial model in the present study, which showed OA development in the medial compartment of the joint just like most cases of human knee OA. Although OA progression in the medial model was similar to or slightly more rapid than that in the posterior cartilage of the mild model, late stage changes including osteophyte formation could be observed. The differences between the Clements model and our medial model are the range of menisectomy and the observation period: partial (about half) menisectomy and 4-week observation for the former, and total menisectomy and 12-week observation for the latter. Creating our medial model in the mutant mice will enable us to examine the effects of these catabolic factors on the OA development not only in the early stage, but also in the later stages, which might be differently regulated. Furthermore, application of combinations of three types of models with ACL transection will elucidate the stage-specific role of the factors in more detail.

The usefulness of the models was demonstrated by immunohistochemistry and ISH of collagens and MMPs, showing that type X collagen and MMP-13 were induced and colocalized in OA cartilage. Articular cartilage is considered to be a permanent cartilage that is free from hypertrophic chondrocytes with type X collagen expression except for the calcified cartilage. In fact, type X collagen localization in the sham-operated knee cartilage was limited to the area below the tidemark; however, in the OA cartilage, type X collagen was strongly expressed in chondrocytes above the tidemark. Previous studies supported the increase in the expression of type X collagen in OA articular chondrocytes, and some reports showed that other ectopic terminal differentiation markers including annexin VI, alkaline phosphatase, osteopontin, and osteocalcin were detected in the OA chondrocytes[24–27]. In the meantime, the expression of MMP-13 that potently degrades cartilage matrix with preference to type II collagen is reported to be upregulated in OA[28,29]. The

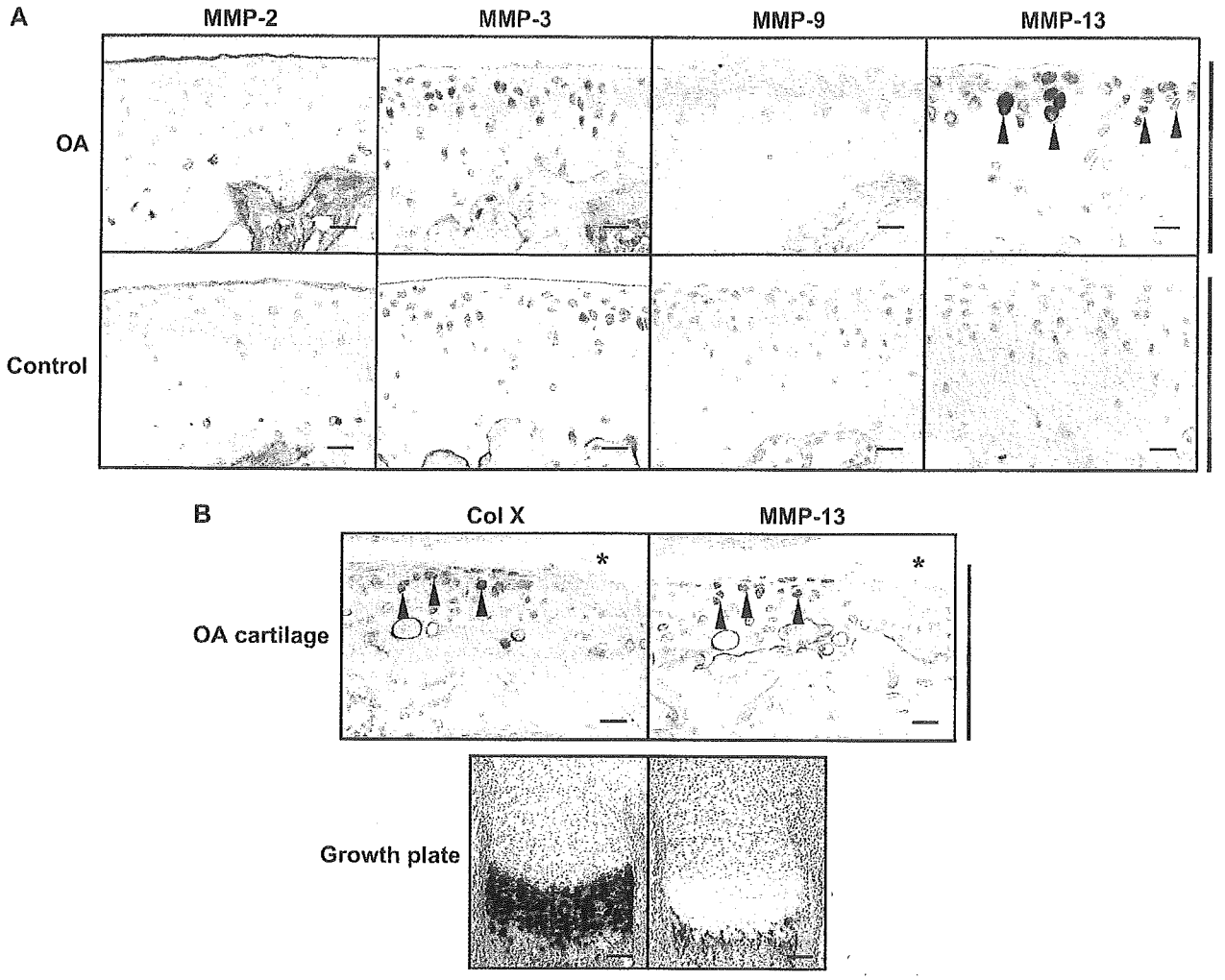

Fig. 7. Immunohistochemistry for MMP-2, -3, -9 and -13 in the OA and control cartilages (A), and the localizations of type X collagen (Col X) and MMP-13 in the OA cartilage and the growth plate (B). Blue, red, green, and black bars indicate superficial zone, middle/deep zones, calcified cartilage, and subchondral bone, respectively. (A) Immunostainings of the OA cartilage in the moderate model and the sham-operated control 2 weeks after surgery. Immunohistochemistry was performed in dewaxed paraffin sections with polyclonal goat antibodies against rabbit MMP-2, -3, -9 and -13 as described in Methods. The sections were counterstained with methylgreen. Scale bar, 50 μm. (B) Top: Immunostainings for Col X and MMP-13 of the OA cartilage in the severe model 4 weeks after surgery. Bottom: ISH for Col X and MMP-13 in the tibial growth plate of mouse embryo (E17.5). In the OA cartilage MMP-13 and Col X (arrowheads) were colocalized in the vicinity of the defect lesion (asterisk), although in the normal growth plate only the highly differentiated subpopulation in the Col X-positive chondrocytes expressed MMP-13. Scale bar, 100 μm.

transgenic mouse expressing constitutively active MMP-13 showed OA changes under physiological conditions[30], suggesting a close relationship between MMP-13 and cartilage destruction in OA. These findings suggest that articular chondrocytes could not maintain characters of a permanent cartilage during OA development, but gained those of a differentiating cartilage such as growth plate and fracture callus. The previous and present studies revealed that in the growth plate there is a strict regulation between type X collagen and MMP-13 expression patterns: only the highly differentiated cells in the type X collagen-positive chondrocytes expressed MMP-13[31,32]. This sequence of expression may be important for the physiological process of endochondral ossification following the cartilage matrix degradation during skeletal growth. However, in OA cartilage, this hierarchy was disrupted: MMP-13 expression was colocalized with that of type X collagen in chondrocytes above the tidemark. We thus speculate that recruitment of abnormal chondrocytes that simultaneously undergo hypertrophic differentiation and MMP-13 expression under the stimulation of mechanical stress may be a key event in the development of OA.

In summary, we established four types of mouse models exhibiting various speeds of OA progression stimulated by mechanical stress. These models were practical, reproducible, and showed pathologic features similar to human OA. And, more importantly, by applying a mouse genomics approach to the models, molecular backgrounds in various stages of OA development could be examined. Hence, the next task will be to apply the models to mice lacking or overexpressing candidate genes. First, we are interested in the OA development in MMP-13-deficient mice. In addition, chondrocyte hypertrophy and MMP-13 remind us of a transcriptional activator Runx2 that is known to positively regulate both of them[33–39]. Although homozygous Runx2-deficient mice died just after birth, the heterozygous

deficient mice developed and grew normally without abnormalities of major organs except for cleidocranial dysplasia[33,40]. Studies creating OA models in these deficient mice are now underway.

References

1. Doherty M. Risk factors for progression of knee osteoarthritis. Lancet 2001;358:775–6.
2. Haywood L, McWilliams DF, Pearson CI, Gill SE, Ganesan A, Wilson D, *et al.* Inflammation and angiogenesis in osteoarthritis. Arthritis Rheum 2003; 48:2173–7.
3. Mollenhauer JA, Erdmann S. Introduction: molecular and biomechanical basis of osteoarthritis. Cell Mol Life Sci 2002;59:3–4.
4. Haq I, Murphy E, Dacre J. Osteoarthritis. Postgrad Med J 2003;79:377–83.
5. Brandt KD. Animal models: insights into osteoarthritis (OA) provided by the cruciate-deficient dog. Br J Rheumatol 1991;30(Suppl 1):5–9.
6. Brandt KD. Animal models of osteoarthritis. Biorheology 2002;39:221–35.
7. Bendele AM. Animal models of osteoarthritis. J Musculoskelet Neuron Interact 2001;1:363–76.
8. Hayami T, Pickarski M, Wesolowski GA, McLane J, Bone A, Destefano J, *et al.* The role of subchondral bone remodeling in osteoarthritis: reduction of cartilage degeneration and prevention of osteophyte formation by alendronate in the rat anterior cruciate ligament transection model. Arthritis Rheum 2004;50: 1193–206.
9. Walton M. Patella displacement and osteoarthrosis of the knee joint in mice. J Pathol 1979;127:165–72.
10. Wilhelmi G, Faust R. Suitability of the C57 black mouse as an experimental animal for the study of skeletal changes due to ageing, with special reference to osteo-arthrosis and its response to tribenoside. Pharmacology 1976;14:289–96.
11. Saamanen AK, Salminen HJ, Dean PB, De Crombrugghe B, Vuorio EI, Metsaranta MP. Osteoarthritis-like lesions in transgenic mice harboring a small deletion mutation in type II collagen gene. Osteoarthritis Cartilage 2000;8:248–57.
12. Dell RB, Holleran S, Ramakrishnan R. Sample size determination. ILAR J 2002;43:207–13.
13. Hoshi K, Komori T, Ozawa H. Morphological characterization of skeletal cells in Cbfa1-deficient mice. Bone 1999;25:639–51.
14. Stoop R, Buma P, van der Kraan PM, Hollander AP, Clark Billinghurst R, Robin Poole A, *et al.* Differences in type II collagen degradation between peripheral and central cartilage of rat stifle joints after cranial cruciate ligament transection. Arthritis Rheum 2000;43: 2121–31.
15. Lee K, Deeds JD, Segre GV. Expression of parathyroid hormone-related peptide and its receptor messenger ribonucleic acids during fetal development of rats. Endocrinology 1995;136:453–63.
16. Helminen HJ, Kiraly K, Pelttari A, Tammi MI, Vandenberg P, Pereira R, *et al.* An inbred line of transgenic mice expressing an internally deleted gene for type II procollagen (COL2A1). Young mice have a variable phenotype of a chondrodysplasia and older mice have osteoarthritic changes in joints. J Clin Invest 1993;92: 582–95.
17. Chambers MG, Bayliss MT, Mason RM. Chondrocyte cytokine and growth factor expression in murine osteoarthritis. Osteoarthritis Cartilage 1997;5: 301–8.
18. Price JS, Chambers MG, Poole AR, Fradin A, Mason RM. Comparison of collagenase-cleaved articular cartilage collagen in mice in the naturally occurring STR/ort model of osteoarthritis and in collagen-induced arthritis. Osteoarthritis Cartilage 2002;10:172–9.
19. Poole AR. An introduction to the pathophysiology of osteoarthritis. Front Biosci 1999;4:D662–70.
20. Santori N, Villar RN. Arthroscopic findings in the initial stages of hip osteoarthritis. Orthopedics 1999;22: 405–9.
21. Mankin HJ, Johnson ME, Lippiello L. Biochemical and metabolic abnormalities in articular cartilage from osteoarthritic human hips. III. Distribution and metabolism of amino sugar-containing macromolecules. J Bone Joint Surg Am 1981;63:131–9.
22. Clements KM, Price JS, Chambers MG, Visco DM, Poole AR, Mason RM. Gene deletion of either interleukin-1beta, interleukin-1beta-converting enzyme, inducible nitric oxide synthase, or stromelysin 1 accelerates the development of knee osteoarthritis in mice after surgical transection of the medial collateral ligament and partial medial meniscectomy. Arthritis Rheum 2003;48:3452–63.
23. Poole AR, Howell DS. Etiopathies of osteoarthritis. In: Moskowitz RW, Howell DS, Altman RD, Buckwalter JA, Goldberg VM, Eds. Osteoarthritis: Diagnosis and Medical/Surgical Management. Philadelphia: Saunders 2001;29–47.
24. von der Mark K, Kirsch T, Nerlich A, Kuss A, Weseloh G, Gluckert K, *et al.* Type X collagen synthesis in human osteoarthritic cartilage. Indication of chondrocyte hypertrophy. Arthritis Rheum 1992; 35:806–11.
25. Boos N, Nerlich AG, Wiest I, von der Mark K, Ganz R, Aebi M. Immunohistochemical analysis of type-X-collagen expression in osteoarthritis of the hip joint. J Orthop Res 1999;17:495–502.
26. Pullig O, Weseloh G, Gauer S, Swoboda B. Osteopontin is expressed by adult human osteoarthritic chondrocytes: protein and mRNA analysis of normal and osteoarthritic cartilage. Matrix Biol 2000;19: 245–55.
27. Pfander D, Swoboda B, Kirsch T. Expression of early and late differentiation markers (proliferating cell nuclear antigen, syndecan-3, annexin VI, and alkaline phosphatase) by human osteoarthritic chondrocytes. Am J Pathol 2001;159:1777–83.
28. Mitchell PG, Magna HA, Reeves LM, Lopresti-Morrow LL, Yocum SA, Rosner PJ, *et al.* Cloning, expression, and type II collagenolytic activity of matrix metalloproteinase-13 from human osteoarthritic cartilage. J Clin Invest 1996;97:761–8.
29. Billinghurst RC, Dahlberg L, Ionescu M, Reiner A, Bourne R, Rorabeck C, *et al.* Enhanced cleavage of type II collagen by collagenases in osteoarthritic articular cartilage. J Clin Invest 1997;99:1534–45.
30. Neuhold LA, Killar L, Zhao W, Sung ML, Warner L, Kulik J, *et al.* Postnatal expression in hyaline cartilage of constitutively active human collagenase-3 (MMP-13) induces osteoarthritis in mice. J Clin Invest 2001;107:35–44.

31. D'Angelo M, Yan Z, Nooreyazdan M, Pacifici M, Sarment DS, Billings PC, *et al.* MMP-13 is induced during chondrocyte hypertrophy. J Cell Biochem 2000; 77:678–93.
32. Jimenez MJ, Balbin M, Alvarez J, Komori T, Bianco P, Holmbeck K, *et al.* A regulatory cascade involving retinoic acid, Cbfa1, and matrix metalloproteinases is coupled to the development of a process of perichondrial invasion and osteogenic differentiation during bone formation. J Cell Biol 2001;155:1333–44.
33. Komori T, Yagi H, Nomura S, Yamaguchi A, Sasaki K, Deguchi K, *et al.* Targeted disruption of Cbfa1 results in a complete lack of bone formation owing to maturational arrest of osteoblasts. Cell 1997;89: 755–64.
34. Inada M, Yasui T, Nomura S, Miyake S, Deguchi K, Himeno M, *et al.* Maturational disturbance of chondrocytes in Cbfa1-deficient mice. Dev Dyn 1999;214: 279–90.
35. Jimenez MJ, Balbin M, Lopez JM, Alvarez J, Komori T, Lopez-Otin C. Collagenase 3 is a target of Cbfa1, a transcription factor of the runt gene family involved in bone formation. Mol Cell Biol 1999;19:4431–42.
36. Porte D, Tuckermann J, Becker M, Baumann B, Teurich S, Higgins T, *et al.* Both AP-1 and Cbfa1-like factors are required for the induction of interstitial collagenase by parathyroid hormone. Oncogene 1999; 18:667–78.
37. Ueta C, Iwamoto M, Kanatani N, Yoshida C, Liu Y, Enomoto-Iwamoto M, *et al.* Skeletal malformations caused by overexpression of Cbfa1 or its dominant negative form in chondrocytes. J Cell Biol 2001;153: 87–100.
38. Takeda S, Bonnamy JP, Owen MJ, Ducy P, Karsenty G. Continuous expression of Cbfa1 in nonhypertrophic chondrocytes uncovers its ability to induce hypertrophic chondrocyte differentiation and partially rescues Cbfa1-deficient mice. Genes Dev 2001;15:467–81.
39. Otto F, Lubbert M, Stock M. Upstream and downstream targets of RUNX proteins. J Cell Biochem 2003;89: 9–18.
40. Otto F, Thornell AP, Crompton T, Denzel A, Gilmour KC, Rosewell IR, *et al.* Cbfa1, a candidate gene for cleidocranial dysplasia syndrome, is essential for osteoblast differentiation and bone development. Cell 1997;89:765–71.

Suppression of Aging in Mice by the Hormone Klotho

Hiroshi Kurosu,[1] Masaya Yamamoto,[1] Jeremy D. Clark,[1] Johanne V. Pastor,[1] Animesh Nandi,[1] Prem Gurnani,[1] Owen P. McGuinness,[3] Hirotaka Chikuda,[4] Masayuki Yamaguchi,[4] Hiroshi Kawaguchi,[4] Iichiro Shimomura,[5] Yoshiharu Takayama,[2] Joachim Herz,[2] C. Ronald Kahn,[6] Kevin P. Rosenblatt,[1] Makoto Kuro-o[1]*

A defect in *Klotho* gene expression in mice accelerates the degeneration of multiple age-sensitive traits. Here, we show that overexpression of *Klotho* in mice extends life span. Klotho protein functions as a circulating hormone that binds to a cell-surface receptor and represses intracellular signals of insulin and insulin-like growth factor 1 (IGF1), an evolutionarily conserved mechanism for extending life span. Alleviation of aging-like phenotypes in Klotho-deficient mice was observed by perturbing insulin and IGF1 signaling, suggesting that Klotho-mediated inhibition of insulin and IGF1 signaling contributes to its anti-aging properties. Klotho protein may function as an anti-aging hormone in mammals.

Klotho was originally identified as a mutated gene in a mouse strain that accelerates age-dependent loss of function in multiple age-sensitive traits (*1*). An insertional mutation that disrupts the 5′ promoter region of the *Klotho* gene resulted in a strong hypomorphic allele. Mice homozygous for the mutated allele ($KL^{-/-}$ mice) appeared normal until 3 to 4 weeks old but then began to manifest multiple age-related disorders observed in humans, including ectopic calcification, skin atrophy, muscle atrophy, osteoporosis, arteriosclerosis, and pulmonary emphysema. $KL^{-/-}$ mice suffered premature death around two months of age.

The *Klotho* gene encodes a single-pass transmembrane protein that is detectable in limited tissues, particularly the distal convoluted tubules in the kidney and the choroid plexus in the brain. Because a defect in the *Klotho* gene leads to systemic age-dependent

[1]Department of Pathology, [2]Department of Molecular Genetics, University of Texas (UT) Southwestern Medical Center at Dallas, 5323 Harry Hines Boulevard, Dallas, TX 75390–9072, USA. [3]Department of Molecular Physiology and Biophysics, Vanderbilt University School of Medicine, 702 Light Hall, Nashville, Tennessee 37232–0615, USA. [4]Department of Sensory and Motor System Medicine, University of Tokyo, 7-3-1 Hongo, Bunkyo, Tokyo 113-8655, Japan. [5]Department of Internal Medicine and Molecular Science, Graduate School of Medicine, Osaka University, 2-2 Yamadaoka, Suita, Osaka 565-0871, Japan. [6]Research Division, Joslin Diabetes Center, Department of Medicine, Harvard Medical School, One Joslin Place, Boston, MA 02215, USA.

*To whom correspondence should be addressed. E-mail: makoto.kuro-o@utsouthwestern.edu

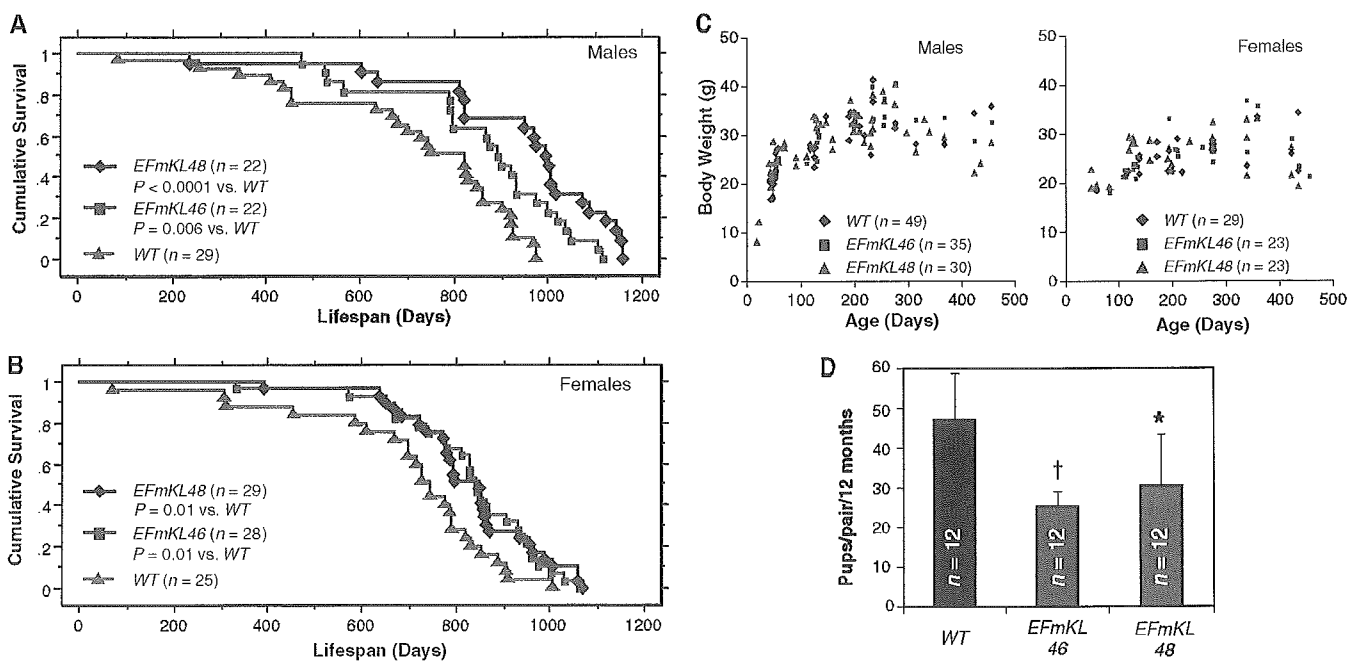

Fig. 1. Klotho overexpression extends life span in the mouse. Kaplan-Meier analysis of survival in (A) males [$P = 0.006$ in *EFmKL46* versus wild-type (WT) mice, and $P < 0.0001$ in *EFmKL48* versus wild type by log-rank test) and in (B) females ($P = 0.01$ in *EFmKL46* versus wild type, and $P = 0.01$ in *EFmKL48* versus wild type by log-rank test). The average life span of male wild-type, *EFmKL46*, and *EFmKL48* mice was 715 ± 44 days, 858 ± 40 days, and 936 ± 47 days (means ± SEM), respectively. The average life span of female wild-type, *EFmKL46*, and *EFmKL48* mice was 697 ± 45 days, 829 ± 32 days, and 830 ± 29 days, respectively. (C) Body weight of wild-type, *EFmKL46*, and *EFmKL48* mice. No significant difference in growth was observed. (D) Klotho overexpression reduces fecundity. Twelve breeding pairs at 12 weeks of age were set up for each genotype. The number of offspring generated during 12 months was recorded for each breeding pair. Although average litter size (pups per birth) of wild-type, *EFmKL46*, and *EFmKL48* pairs was not significantly different (6.6 ± 1.0, 6.1 ± 1.3, and 7.0 ± 1.2, respectively), the number of births (births per pair per 12 months) was fewer in transgenic mice pairs (7.2 ± 1.6, 4.2 ± 0.8, and 4.5 ± 2.2, respectively), resulting in significantly fewer offspring in transgenic pairs. Data are means ± SD. *, $P < 0.05$; †, $P < 0.01$ versus wild-type mice by analysis of variance (ANOVA).

degeneration, the Klotho protein may function through a circulating humoral factor that regulates the development of age-related disorders or natural aging processes (*2*). Notably, some single-nucleotide polymorphisms in the human *KLOTHO* gene are associated with altered life span (*3*) and altered risk for coronary artery disease (*4*), osteoporosis (*5*–*7*), and stroke (*8*).

Little is known about Klotho protein function and the molecular mechanism by which it suppresses the development of aging-like phenotypes. The extracellular domain of Klotho protein is composed of two internal repeats, KL1 and KL2, that share amino acid sequence homology to β-glucosidases of bacteria and plants (20 to 40% identity) (*1*). However, glucosidase activity is not present in recombinant Klotho protein (*9*), and the essential glutamate residue at the β-glucosidase active center is replaced with asparagine and alanine in KL1 and KL2, respectively (*10*). Here, we demonstrate that *Klotho* is an aging suppressor gene whose product functions as a hormone that inhibits intracellular insulin and IGF1 signaling.

Klotho overexpression extends life span in mice. We previously generated independent transgenic lines of mice that overexpress *Klotho* under the control of the human elongation factor 1α promoter (*1*) (*EFmKL46* and *EFmKL48*) (fig. S1). Here, we compared the life span of the transgenic mice with that of wild-type controls that are near-coisogenic by virtue of backcrossing onto the C3H background four times. Each line was previously confirmed to express functional Klotho protein from the transgene (*1*). Mice carrying the

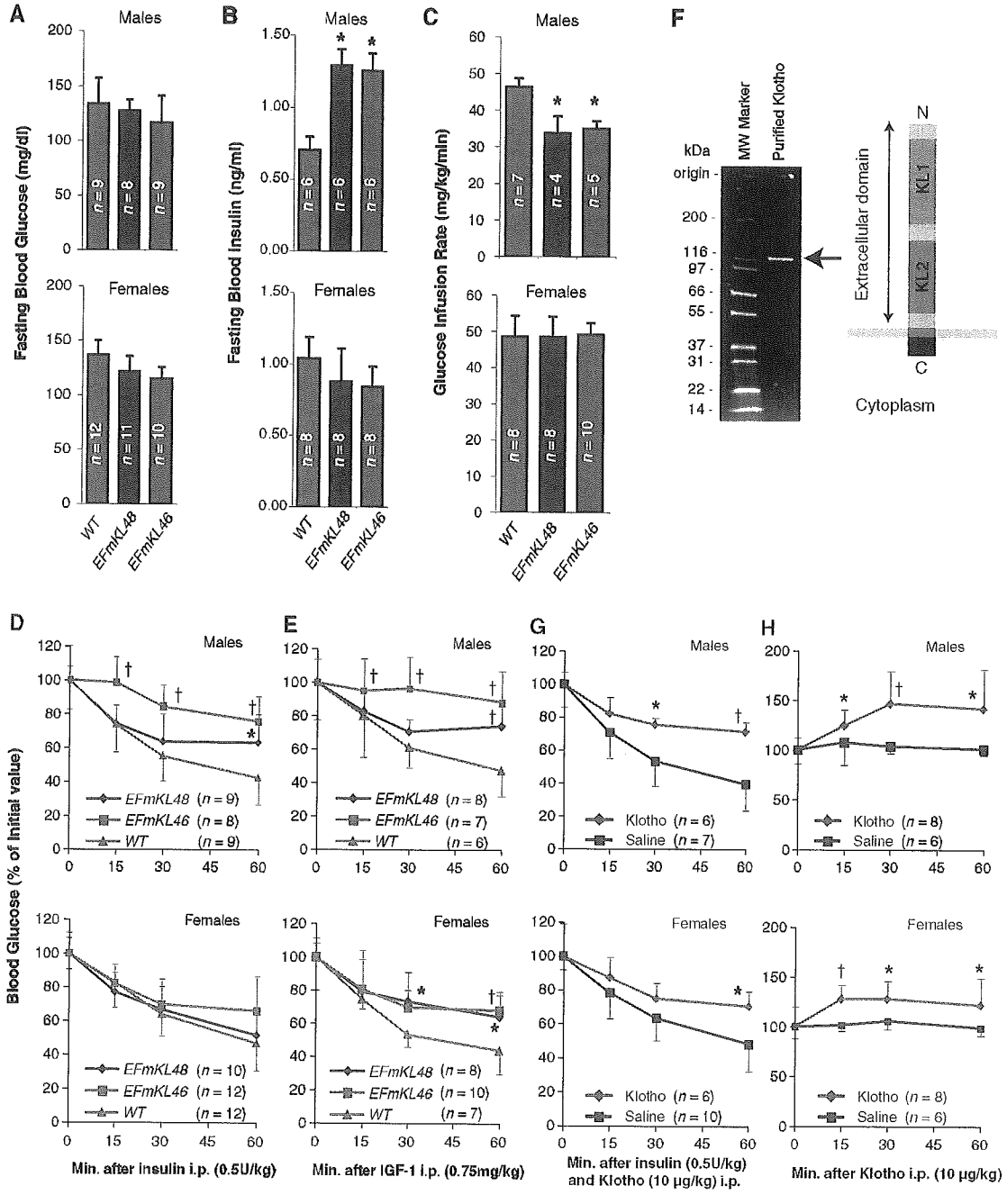

Fig. 2. Klotho increases resistance to insulin and IGF1. (**A** and **B**) Fasting blood glucose (A) and insulin (B) levels were compared between wild-type (WT), *EFmKL48*, and *EFmKL46* mice. (**C**) Hyperinsulinemic euglycemic clamp experiments. Glucose infusion rate (mg/kg/min) was compared between wild-type, *EFmKL48*, and *EFmKL46* mice. During the clamp experiments there were no differences in blood glucose concentration between wild-type, *EFmKL46*, and *EFmKL48* mice. The number of animals (*n*) for each group is indicated in the bars. (**D** and **E**) Insulin (D) and IGF1 (E) tolerance tests. Blood glucose levels after injection of insulin (0.5 U/kg) or IGF1 (0.75 mg/kg) were expressed as a percentage change from blood glucose concentration at time zero. Error bars indicate SD. *, $P < 0.05$ and †, $P < 0.01$ versus wild-type mice by ANOVA. (**F**) A schematic representation of Klotho extracellular peptide (right) and analysis of purified recombinant Klotho peptide by SDS-polyacrylamide gel electrophoresis (left). (**G**) The effect of Klotho injection on insulin tolerance in mice. Insulin tolerance tests were performed with age-matched wild-type mice immediately after intraperitoneal injection with saline or purified recombinant Klotho peptide (10 μg/kg). (**H**) The effect of Klotho injection on blood glucose levels. Saline or Klotho protein (10 μg/kg) was administered into age-matched wild-type mice by intraperitoneal injection. Error bars indicate SD. *, $P < 0.05$ and †, $P < 0.01$ versus saline-injected mice by ANOVA.

EFmKL46 or *EFmKL48* transgenic alleles, fed *ad libitum*, outlived wild-type controls by 20.0 and 30.8%, respectively, in males (Fig. 1A) and by 18.8 and 19.0%, respectively, in females (Fig. 1B).

Caloric restriction is associated with increased longevity in various species (*11*). To assess whether mice overexpressing Klotho were restricting their own diets, we monitored food intake and oxygen consumption in transgenic and wild-type mice for 24 hours at 32 to 36 weeks of age. No significant differences in these parameters were observed (table S1). Small body size is also associated with extended longevity in diet-restricted mice and in mice that are mutant for pituitary or growth hormone receptor function (*12*, *13*). However, we did not observe any substantial difference in growth between *EFmKL46*, *EFmKL48*, and wild-type mice (Fig. 1C). Both *EFmKL46* and *EFmKL48* breeding pairs generated fewer offspring than wild-type breeding pairs (Fig. 1D). As expected from the evolutionary theory of longevity, maximum fitness of the organism is a trade-off between life span and fertility (*14*). These data indicate that *Klotho* systemically modulates aging through mechanisms independent of food intake and growth, but potentially in association with reproduction.

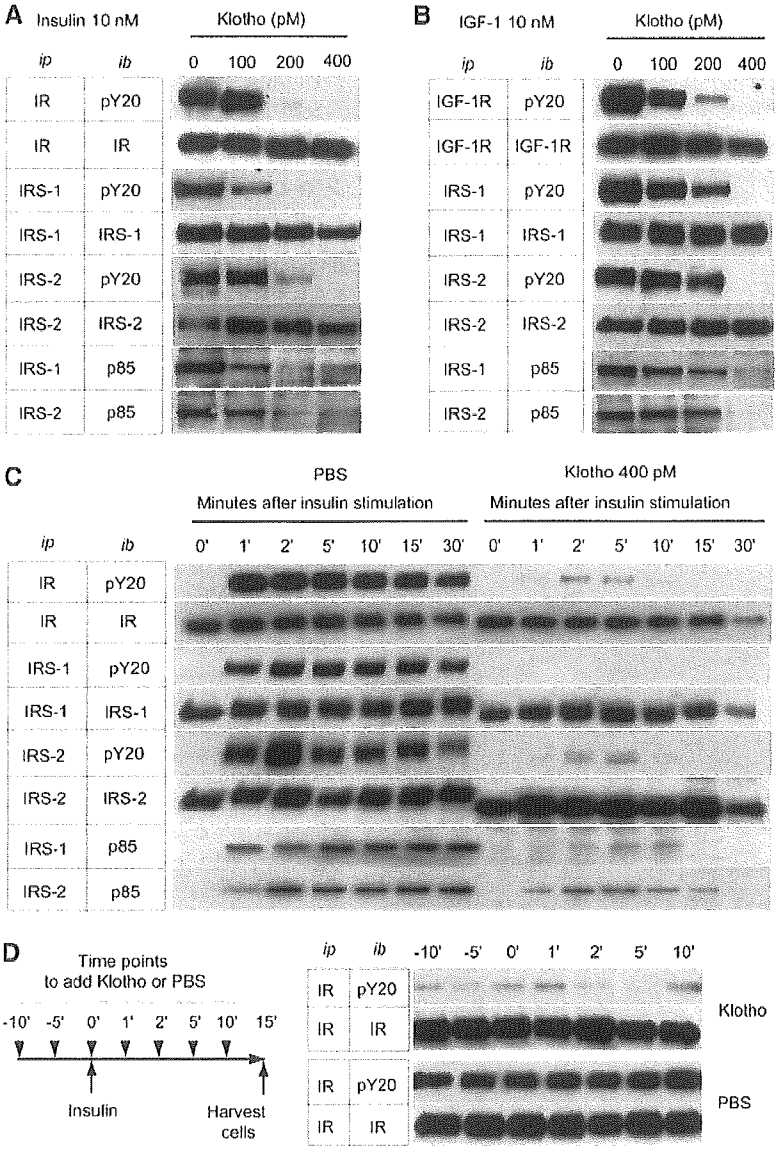

Fig. 3. Klotho protein inhibits intracellular insulin and IGF1 signaling. (**A** and **B**) Effect of Klotho on tyrosine phosphorylation of insulin and IGF1 receptors as well as IRS-1 and IRS-2, association of IRS-1 and IRS-2 with the PI3-kinase regulatory subunit (p85), and phosphorylation of Akt in L6 cells stimulated with 10 nM of insulin (A) or 10 nM of IGF1 (B). Antibodies used for immunoprecipitation (ip) and immunoblotting (ib) were indicated. IR, antibody to insulin receptor β chain; pY20, antibody to phosphotyrosine; IRS-1, antibody to IRS-1; IRS-2, antibody to IRS-2; p85, antibody to PI3-kinase regulatory subunit; IGF-1R, antibody to IGF1 receptor β chain. (**C**) A time course of the inhibitory effect of Klotho protein (400 pM) on insulin signaling in H4IIE cells. The cells were harvested before (0') and at the indicated time points after insulin stimulation (10 nM). (**D**) Inactivation of activated insulin receptor by Klotho protein. H4IIE cells were stimulated with insulin (10 nM) at time 0' and harvested 15 min later. Klotho (400 pM) or phosphate-buffered saline (PBS) was added at the indicated time points indicated (left panel). The cell lysates were immunoprecipitated with IR and immunoblotted with pY20 or IR (right panel).

Klotho increases resistance to insulin and IGF1. Many genetic data demonstrate that inhibited insulin and IGF1 signaling extends life span in animals from *C. elegans*, to *Drosophila*, to mice (*15*–*21*). Because Klotho must mediate aging through effects of a systemic hormone, we investigated whether the *Klotho* gene is involved in the inhibition of insulin or IGF1 signaling. Mice defective in *Klotho* gene expression have reduced blood glucose and insulin levels coupled with enhanced sensitivity to insulin (*22*).

We compared glucose metabolism in the Klotho-overexpressing transgenic mice with wild-type animals. Blood glucose levels were normal in each transgenic line (Fig. 2A). However, male *EFmKL46* and *EFmKL48* mice had higher blood insulin levels than did wild-type males (Fig. 2B), suggesting that the male transgenic mice are somewhat insulin resistant. We directly assessed sensitivity to insulin with a hyperinsulinemic euglycemic clamp (*23*). As expected, male *EFmKL46* and *EFmKL48* mice required lower glucose infusion rates than did wild-type males to maintain normal blood glucose levels (Fig. 2C). Furthermore, insulin and IGF1 tolerance tests revealed significant attenuation in hypoglycemic response to injected insulin and IGF1 in male transgenic mice (Fig. 2, D and E). Although we were unable to detect insulin resistance in female transgenic mice (Fig. 2, C and D), they were significantly resistant to IGF1 (Fig. 2E). These studies demonstrate that Klotho overexpression induces resistance to insulin and IGF1.

Klotho functions as a hormone. The extracellular domain of Klotho is shed on the cell surface and detected in the blood and cerebrospinal fluid in mice and humans (*24*). Immunoblot analysis of plasma with the use of rabbit anti-Klotho antiserum demonstrated that the extracellular Klotho peptide can be detected in wild-type, *EFmKL48*, and *EFmKL46* mice but not in $KL^{-/-}$ mice (fig. S2). Radioimmunoassay further demonstrated that Klotho peptide is ~100 pM in wild-type mice and about two times as high in the transgenic overexpression strains (fig. S3). The extracellular domain of Klotho may function as a hormone-like substance (*2*).

To assess the function of the Klotho extracellular peptide, we generated a soluble form of recombinant Klotho protein comprising the 952–amino acid extracellular domain, and de-